

RESEARCH ARTICLE

10.1002/2016JE005110

Key Points:

- We explore radar attenuation for a variety of potential thermal structures of Europa's shell and two end-member attenuation models
- We show that the deepest signal penetration is possible through cold downwellings with direct ocean detection for shells of up to 15 km
- Our results support the possibility to detect the eutectic isotherm for all plausible shell thicknesses

Supporting Information:

- Supporting Information S1

Correspondence to:

K. Kalousová,
kalous@karel.troja.mff.cuni.cz

Citation:

Kalousová, K., D. M. Schroeder, and K. M. Soderlund (2017), Radar attenuation in Europa's ice shell: Obstacles and opportunities for constraining the shell thickness and its thermal structure, *J. Geophys. Res. Planets*, 122, 524–545, doi:10.1002/2016JE005110.

Received 17 JUN 2016

Accepted 11 JAN 2017

Accepted article online 18 JAN 2017

Published online 20 MAR 2017

Radar attenuation in Europa's ice shell: Obstacles and opportunities for constraining the shell thickness and its thermal structure

Klára Kalousová^{1,2}, Dustin M. Schroeder³, and Krista M. Soderlund⁴
¹Jet Propulsion Laboratory, California Institute of Technology, Pasadena, California, USA, ²Department of Geophysics, Faculty of Mathematics and Physics, Charles University, Prague, Czech Republic, ³Department of Geophysics, School of Earth, Energy, and Environmental Sciences, Stanford University, Stanford, California, USA, ⁴Institute for Geophysics, John A. and Katherine G. Jackson School of Geosciences, University of Texas at Austin, Austin, Texas, USA

Abstract Young surface and possible recent endogenic activity make Europa one of the most exciting solar system bodies and a primary target for spacecraft exploration. Future Europa missions are expected to carry ice-penetrating radar instruments designed to investigate its subsurface thermophysical structure. Several authors have addressed the radar sounders' performance at icy moons, often ignoring the complex structure of a realistic ice shell. Here we explore the variation in two-way radar attenuation for a variety of potential thermal structures of Europa's shell (determined by reference viscosity, activation energy, tidal heating, surface temperature, and shell thickness) as well as for low and high loss temperature-dependent attenuation model. We found that (i) for all investigated ice shell thicknesses (5–30 km), the radar sounder will penetrate between 15% and 100% of the total thickness, (ii) the maximum penetration depth varies laterally, with deepest penetration possible through cold downwellings, (iii) direct ocean detection might be possible for shells of up to 15 km thick if the signal travels through cold downwelling ice or the shell is conductive, (iv) even if the ice/ocean interface is not directly detected, penetration through most of the shell could constrain the deep shell structure through returns from deep non-ocean interfaces or the loss of signal itself, and (v) for all plausible ice shells, the two-way attenuation to the eutectic point is $\lesssim 30$ dB which shows a robust potential for longitudinal investigation of the ice shell's shallow thermophysical structure.

1. Introduction

With its dearth of large impact craters that indicates a strikingly young surface of less than 100 Myr [e.g., Bierhaus *et al.*, 2009] and the abundance of unique tectonic and cryovolcanic features that points to a relatively recent endogenic activity [e.g., Kattenhorn and Hurford, 2009; Collins and Nimmo, 2009], Europa is one of the most exciting planetary bodies within our solar system. Gravity data collected by the Galileo spacecraft indicate that the satellite interior is differentiated into a metallic core, a silicate mantle, and an outer H₂O layer, approximately 80–170 km thick [Anderson *et al.*, 1998]. Surface geology hinted at the existence of a buried liquid water ocean [e.g., Carr *et al.*, 1998; Pappalardo *et al.*, 1999], but the most compelling evidence that Europa possesses a global salty ocean underneath its ice shell was the detection of an induced magnetic field by the Galileo magnetometer [Khurana *et al.*, 1998; Kivelson *et al.*, 2000]. Still, the current ice shell thickness, as well as its thermal state (convective or conductive), remains poorly constrained, with the shell thickness estimates ranging from a few kilometers to more than 40 km [e.g., Ojakangas and Stevenson, 1989; Golombek and Banerdt, 1990; Williams and Greeley, 1998; McKinnon, 1999; Hussmann *et al.*, 2002; Nimmo *et al.*, 2003; Billings and Kattenhorn, 2005].

Europa is locked in Laplace resonance with its neighbors Io and Ganymede, which results in nonzero eccentricities and leads to significant tidal deformations within the interior of these bodies [e.g., Greenberg, 1987]. The associated tidal heating may be several times larger than radiogenic heating in the rocky core and might prevent Europa's ocean from freezing completely [Sotin *et al.*, 2009].

Morphological analyses of chaos terrains [Schmidt *et al.*, 2011] and double ridges [Dombard *et al.*, 2013] suggest the presence of shallow lenses of water or brines, perched only a few kilometers below Europa's cold brittle surface. However, it is not clear if liquid water can accumulate in the upper part of Europa's ice shell for long enough [e.g., Tobie *et al.*, 2003; Kalousová *et al.*, 2014, 2016]. Nevertheless, recent detections of water

vapor over Europa's south pole [Roth *et al.*, 2014; Sparks *et al.*, 2016] suggest the existence of an ongoing plume activity similar to that observed at Enceladus [e.g., Hansen *et al.*, 2006], and detection of salts [McCord *et al.*, 1998; Brown and Hand, 2013] and hydrated sulfuric acid [Carlson *et al.*, 1999] on Europa's surface indicates the presence of chemical elements essential for biology.

Powered by tides, the endogenic activity in a chemically rich environment together with an expected ocean-mantle contact may provide key ingredients for life [e.g., Hand *et al.*, 2009], which makes Europa one of the best candidates for habitability and a primary target for future explorations. Indeed, two missions were recently selected to revisit Europa—European Space Agency's (ESA) JUPITER ICy moons Explorer (JUICE) [Grasset *et al.*, 2013] will perform two targeted Europa flybys and NASA's planned Europa Multiple Flyby Mission [Pappalardo *et al.*, 2015] is a Europa targeted mission with an estimate of 45 flybys. The scientific payloads of both of these missions contain ice-penetrating radar instruments which are powerful tools to investigate the subsurface structure of the ice shell. The expected outcome of radar sounding of Europa's subsurface can be compared to the impact of seismic tomography on our knowledge of the structure of Earth's interior. For the JUICE mission, the RIME instrument (Radar for Icy Moons Exploration) has been chosen to study the subsurface structure of the Galilean moons. It will operate in a single frequency band centred at 9 MHz with a bandwidth of 3 MHz [Bruzzone *et al.*, 2015]. NASA's spacecraft will carry the REASON instrument (Radar for Europa Assessment and Sounding: Ocean to Near-surface), a dual frequency instrument with center frequencies of 9 MHz (bandwidth of 1 MHz) and 60 MHz (bandwidth of 10 MHz) [Blankenship *et al.*, 2009; Grima *et al.*, 2015]. Its primary aims will be to characterize the distribution of shallow subsurface water as well as the thermophysical structure of Europa's ice shell and to search for the ice/ocean interface.

While the RIME and REASON instruments are going to be the first to sound the outer solar system bodies, sounding of Earth's ice sheets and ice caps by airborne ice-penetrating radar is now well established and constitutes the principal means to constrain their inner structure, bedrock interface properties, and presence of subglacial lakes [e.g., Oswald and Robin, 1973; Dowdeswell and Evans, 2004; Bingham and Siegert, 2007; Peters *et al.*, 2007; MacGregor *et al.*, 2013; Schroeder *et al.*, 2014]. Recently, orbital radar sounding has been successfully applied also on the other inner solar system targets: ESA's MARSIS (Mars Advanced Radar for Subsurface and Ionosphere Sounding) instrument [Picardi *et al.*, 2005] on board the Mars Express spacecraft detected the interface between the bottom of the south polar cap and the bedrock [Plaut *et al.*, 2007], and NASA's SHARAD (SHAlow RADar) instrument [Seu *et al.*, 2007] carried by the Mars Reconnaissance Orbiter revealed the detailed internal stratified structures of the north polar cap [Phillips *et al.*, 2008]. However, all planetary ice masses that have been sounded (i.e., the ice sheets or polar caps on the Earth and Mars) were able to be sounded to their bottom due to relatively small thicknesses of a few kilometers. The shell of Europa is likely thicker which might result in large differences in the portion of the ice mass that could be penetrated.

Due to high transparency of ice at radar frequencies, the sounding instruments have the capability to penetrate deep into the subsurface of icy bodies. The radar waves traveling through the ice shell interact with subsurface structures associated with dielectric contrasts that can include transitions in density, chemistry, phase, temperature, and crystal structure within the ice column [Dowdeswell and Evans, 2004]. These interactions result in detectable radar return. While losses due to scattering from voids and/or water pockets are not expected to be a significant obstacle to sounding, the attenuation in warm ductile ice might significantly reduce the penetration. The potential performance of ice-penetrating radar in sounding Europa's ice shell has been investigated by several authors. Chyba *et al.* [1998] estimated radar signal attenuation for different thermal profiles (conductive and convective) with various mixtures of pure ice and lunar soil and found an ice/ocean interface detectability limit of about 10 km. Moore [2000] and later Blankenship *et al.* [2009] considered a different composition and three distinct shell thicknesses corresponding to different ice formation processes and thermal profiles. They found that for shell thicknesses around 10 km or smaller with conductive thermal profiles, the total signal absorption is less than an instrumental range and the ice/ocean interface should be detectable. For thicker shells in the convective regime, the estimated absorption became too high, indicating that the electromagnetic waves would not be able to penetrate the whole shell to the interface with the ocean. Moore [2000] has further shown that in the case of conductive shells, the penetration depth is almost insensitive to the shell thickness since nearly all of the losses are caused by the warmest part of the ice. Finally, McKinnon [2005] compared attenuation in cold and hot parts of the convecting shell and showed that the cold downwellings would be highly favorable for the radar signal propagation which raised the possibility for the detection of subsurface interfaces deeper than the 10 km penetration depth suggested by the earlier study. This work was the first to indicate the problem with concept of a single global penetration

depth value as a metric of instrument performance, since upwelling and downwelling penetrations can be quite different. These results were later confirmed by *Di Paolo et al.* [2014]. Recently, *Di Paolo et al.* [2016] used information from experimental measurements of icy materials' dielectric properties as well as from numerical models of thermal states and radar signal propagation. They evaluated the modeled radar response in terms of attenuation, signal-to-noise ratio, and reflectivity and concluded that the ice/ocean interface should be detectable by radar sounder up to a depth of 15 km if Europa's shell is conductive and 12 km if the shell is convective (and the radar signal travels through a cold downwelling). However, *Di Paolo et al.* [2016] do not extend their treatment of the detectability of ice/ocean (and internal) interfaces to explore the horizontal and vertical structure of radar attenuation as a function of ice shell parameters. This is important because attenuation is not only an obstacle to detection of subsurface dielectric interfaces but is itself an interpretable geophysical signal.

In this study, we extend the work of *McKinnon* [2005] and *Di Paolo et al.* [2016] by considering a broader range of model parameters (shell thickness, ice viscosity, tidal heating, and surface temperature) in order to obtain an envelope of plausible thermal states and the corresponding attenuation profiles. We also investigate the full horizontal structure of temperature and attenuation (both as an obstacle and as a signal) which was not treated in the previous work. Finally, this study provides the first direct treatment of attenuation to the eutectic temperature. The structure of the paper is as follows: in section 2 we summarize the attenuation models used throughout this paper, while in section 3 we provide a brief overview of the solid-state thermal convection numerical model used to determine the thermal states. Our results are described in section 4 and discussed in section 5. Finally, the implications of our results for the performance of ice-penetrating radar in Europa's ice shell are summarized in section 6.

2. Radar Attenuation

The electromagnetic waves emitted by the orbiting radar instrument will be reflected, scattered, and attenuated during their propagation through Europa's icy shell. The power $P_r(d)$ returned from a buried interface at depth d measured by an airborne radar instrument can be written as [cf. *Gudmandsen*, 1971]:

$$P_r(d) = \frac{R(d) A_2(d) B(d) \Psi(d)}{G(d)} P_e, \quad (1)$$

with $R(d)$ the interface reflectivity, $A_2(d)$ the two-way attenuation along the propagation path, $B(d)$ the birefringence, $\Psi(d)$ the total (two-way) transmission after multiple reflections, $G(d)$ the geometric spreading, and P_e the irradiated effective power corrected for the system gain (azimuth and range compressions). In terrestrial polar ices sounding, $\Psi(d) \sim 1$ [*MacGregor et al.*, 2007], while the birefringence $B(d)$ is usually assumed to be depth independent [*Matsuoka et al.*, 2010] and the geometric spreading factor is approximately constant for a fixed spacecraft altitude $H \gg d$. Considering the same approximations for sounding of Europa's interior, equation (1) can be simplified as [e.g., *Pettinelli et al.*, 2015; *Di Paolo et al.*, 2016]:

$$P_r(d) \simeq R(d) A_2(d) P_c, \quad (2)$$

where P_c is the irradiated power corrected for geometric spreading losses and birefringence. Since both the attenuation and reflection coefficients depend on the physical and geological properties encountered along the propagation path, the data acquired by the radar sounder can be used to extract the information about Europa's subsurface.

For the purpose of this study, we assume that a nominal radar sounder could potentially detect a subsurface as long as it experiences less than ~ 100 dB of two-way attenuation in the ice. For example, a radar sounding signal transmitted with peak power ~ 140 dB above the background noise with ~ 100 dB of geometric spreading losses, ~ 35 dB of pulse compression gain, ~ 20 dB of azimuth processing gain, and ~ 10 dB of antenna gain would still have a signal-to-noise ratio of ~ 5 dB after 100 dB of attenuation. While the exact numbers in the link budget will depend on the final instrument design, operational scenario, subsurface dielectric contrast, surface roughness, and signal-to-noise ratio detectability threshold, these values are in family with values found in the literature [e.g., *Blankenship et al.*, 2009; *Bruzzzone et al.*, 2015; *Di Paolo et al.*, 2016]. The volume scattering generated by structural heterogeneities especially in the upper parts of the ice shell is likely to be small at 60 MHz and negligible at 9 MHz [*Aglyamov et al.*, 2017] and is therefore neglected in the

Table 1. Model Parameters

Symbol	Physical Property	Value	Unit
α	thermal expansivity ^a	1.6×10^{-4}	K ⁻¹
κ	thermal diffusivity ^a	10^{-6}	m ² s ⁻¹
g	gravity	1.32	m s ⁻²
η_0	melting point viscosity ^b	$10^{13}, 10^{14}, 10^{15}$	Pa s
R	universal gas constant	8.314	J K ⁻¹ mol ⁻¹
D	ice shell thickness ^b	5, 10, 15, 20, 25, 30	km
ρ	density ^a	920	kg m ⁻³
T_s	surface temperature ^c	50, 100	K
$T_b = T_m$	bottom (melting) temperature	270	K
H_m	maximum heating amplitude ^d	5×10^{-6}	W m ⁻³
η_m	viscosity maximizing volumetric heating	1.5×10^{14}	Pa s
E_a	activation energy of ice viscosity ^b	2.2, 50, 60	kJ mol ⁻¹
T_r	reference temperature ^e	251	K
k_B	Boltzmann constant	8.6173×10^{-5}	eV K ⁻¹
σ_0^0	electrical conductivity of pure ice ^e	9.2	$\mu\text{S m}^{-1}$
C_0	auxiliary constant ^e	1	-
E_0	activation energy of pure ice ^e	0.51	eV
σ_1^0	molar electrical conductivity of acid ice ^e	3.2	S m ⁻¹ M ⁻¹
C_1	radar effective molar concentration of acid ^e	1.2	μM
E_1	activation energy of acid ice ^e	0.20	eV
σ_2^0	molar electrical conductivity of salty ice ^e	0.43	S m ⁻¹ M ⁻¹
C_2	radar effective molar concentration of salt ^e	4.1	μM
E_2	activation energy of salty ice ^e	0.19	eV

^aLide [2004].^bRange of admissible values [e.g., Mitri and Showman, 2005; Showman and Han, 2005].^cPolar and average values [Ojakangas and Stevenson, 1989].^dTobie et al. [2003].^eMatsuoka et al. [2012].

present study. Finally, we assume a flat surface (thus, neglecting the surface clutter) although the two-way propagation through a rough ice surface will result in additional losses (depending on the permittivity of the near surface) [cf., e.g., Grima et al., 2014; Schroeder et al., 2016]. This neglect is motivated by the fact that the rough surface will shift the spatial pattern of attenuation by a constant value of ~ 5 –15 dB (depending on the sounding frequency) [cf., e.g., Di Paolo et al., 2016] in the same way as the unknown radar system and operational parameters (cf. above). Since we are mostly interested in that spatial pattern, we therefore assume the losses due to surface scattering to be already included in our assumed 100 dB maximum attenuation value and neglect them in the attenuation calculations.

In the high frequency and very high frequency bands used in terrestrial and planetary radar sounders, the (one-way) englacial attenuation A_1 (in dB/km) is proportional to the electrical conductivity of ice σ [e.g., Matsuoka et al., 2012]:

$$A_1 = \frac{1000(10 \log_{10} e)}{c \epsilon_0 \sqrt{\epsilon_r}} \sigma \approx 0.914 \sigma, \quad (3)$$

with c the speed of light, ϵ_0 the permittivity of free space, $\epsilon_r = 3.2$ the relative permittivity of pure ice, and the electrical conductivity σ in microsiemens. Ice conductivity in terrestrial ice sheets in turn depends on the contributions from pure ice ($i = 0$) and the impurity content, mainly acids ($i = 1$) and sea salt ($i = 2$), with each component having an Arrhenius-like temperature dependence [e.g., Corr et al., 1993]:

$$\sigma = \sum_{i=0}^2 \sigma_i^0 C_i \exp \left[-\frac{E_i}{k_B} \left(\frac{1}{T} - \frac{1}{T_r} \right) \right]. \quad (4)$$

Here σ_i^0 is the pure ice conductivity ($i = 0$) or molar conductivities ($i = 1, 2$) at the reference temperature $T_r = 251$ K, C_i are the molar concentrations (with $C_0 = 1$), E_i are the activation energies, T is the actual ice temperature, and k_B is the Boltzmann constant. Let us note that σ_i^0 and E_i are frequency independent within the sounding range [Fujita *et al.*, 2000].

To constrain the plausible range of attenuations within Europa's shell, we assume two different attenuation models in this study: "low loss" ice by taking only the first ($i = 0$) contribution in equation (4) and "high loss" ice by taking all three contributions. We chose to represent the high loss case by the values obtained for Siple Dome, Antarctica [Matsuoka *et al.*, 2012], because the corresponding attenuation was larger than all of the doped cases from the review by Pettinelli *et al.* [2015]. Similarly, we chose pure ice as the low loss case since it resulted in lower attenuations than other cases in that study. Therefore, we believe that our chosen models represent the bounding cases for the range of likely impurities, based on the work of Pettinelli *et al.* [2015]. Values of all parameters are specified in Table 1.

The two-way attenuation along the path to and from the interface at depth d is then calculated as:

$$A_2(d) = \sum_{i=0}^{i_d} 2A_1(d_i)\Delta d, \quad (5)$$

where i_d corresponds to the final depth d , $A_1(d_i)$ are the one-way attenuations at depths smaller than d , and Δd is the thickness of each layer in which A_1 is evaluated.

3. Numerical Model of Thermal Convection in Europa's Ice Shell

To assess the possible thermal state of Europa's ice shell, we use the classical Boussinesq approximation (except for the temperature-dependent viscosity and spatially variable volumetric heating) and write the governing equations of solid-state thermal convection in nondimensional form as follows:

$$\nabla \cdot \mathbf{v} = 0, \quad (6)$$

$$0 = -\nabla p + \nabla \cdot (\eta(\nabla \mathbf{v} + \nabla^T \mathbf{v})) - Ra T \mathbf{e}_z \quad (7)$$

$$\frac{\partial T}{\partial t} + \mathbf{v} \cdot \nabla T = \nabla^2 T + H. \quad (8)$$

Here \mathbf{v} is the velocity, p is the dynamic pressure, η is the temperature-dependent viscosity (specified below), ∇^T denotes the transposition, T is the temperature, \mathbf{e}_z is the unit vector in direction of the vertical axis, t is the time, H is the volumetric heating (specified below and considered only in certain simulations), and Ra is the Rayleigh number, defined as:

$$Ra = \frac{\alpha g \rho \Delta T D^3}{\kappa \eta_0}, \quad (9)$$

with α the thermal expansivity, g the surface gravity, ρ the density, $\Delta T = T_b - T_s$ the temperature contrast across the shell, D the shell thickness, κ the thermal diffusivity, and η_0 the reference (melting point) viscosity. The dimensionless parameter Ra represents the ratio of thermal buoyancy to heat and momentum diffusion.

The viscosity of ice is highly nonlinear with at least four known deformational mechanisms (diffusion creep, dislocation creep, grain boundary sliding, and basal slip) [cf. Durham *et al.*, 2001; Goldsby and Kohlstedt, 2001], each of which is, in general, dependent on temperature, pressure, grain size, and stress. Moreover, possible presence of interstitial liquid water might significantly decrease the viscosity values [cf. De La Chapelle *et al.*, 1999]. The aim of this study is to assess the depth of detectable subsurface returns of a radar sounder based on the evaluation of the attenuation profiles where thermochemical effects play the dominant role. Thus, for the sake of simplicity, we consider only temperature-dependent Newtonian viscosity in the Arrhenius form [e.g., Kirk and Stevenson, 1987; Showman and Han, 2004; Tobie *et al.*, 2005; Běhouňková *et al.*, 2012]:

$$\eta = \eta_0 \exp \left[\frac{E_a}{RT_m} \left(\frac{T_m}{T} - 1 \right) \right], \quad (10)$$

with η_0 the melting point viscosity, E_a the activation energy, R the universal gas constant, and T_m the melting temperature. Values of η_0 and E_a are varied in order to capture a broader range of possible thermal states.

In some of the simulations, volumetric shear heating due to tides is considered. Following *Tobie et al.* [2003], we parametrize it as:

$$H = \frac{2H_m}{\frac{\eta}{\eta_m} + \frac{\eta_m}{\eta}}, \quad (11)$$

with H_m the maximum heating amplitude and $\eta_m = G/\omega$ the viscosity for which the heating is maximized (with G the shear modulus and ω the orbital frequency). We use $H_m = 5 \times 10^{-6} \text{ W m}^{-3}$ that corresponds to the mean value for Europa [cf. *Tobie et al.*, 2003] and $\eta_m = 1.5 \times 10^{14} \text{ Pa s}$ corresponding to Europa's orbital frequency. In some simulations with volumetric heating, melting temperature is reached in the convective portion of the shell. However, we do not treat melt generation and transport in this study, but we merely fix the temperature on the melting point and discuss the implications of this treatment in section 5.2. Simulations with no volumetric heating ($H_m = 0 \text{ W m}^{-3}$) are thought of as representative for the situation when volumetric heating is much smaller and therefore negligible. While all model parameters (summarized in Table 1) are assumed constant across the shell throughout section 4 (except for viscosity), we address the effect of temperature-dependent thermal conductivity k in section 5.1.

The governing equations are solved in the Cartesian box of aspect ratio 2 with free slip condition on all boundaries, fixed temperatures at the top and bottom boundaries, and zero normal heat flux through the side boundaries. We will discuss the effect of the prescribed aspect ratio and mechanical boundary conditions on our results in section 5.5. All simulations are started from a purely conductive solution with a small ($\delta T = 0.175 \text{ K}$) perturbation in the temperature field. The steady state (simulations with smaller values of Rayleigh number) or statistical steady state (simulations with larger values of Ra) temperature fields are used to evaluate the attenuation profiles.

The problem is implemented in the open source finite element software package FEniCS (<http://fenicsproject.org>) [Logg et al., 2012; Alnæs et al., 2015] using the Taylor-Hood elements (i.e., piecewise linear functions for the dynamic pressure and piecewise quadratic functions for the velocity) [cf. *Taylor and Hood*, 1973] for the Stokes problem, piecewise quadratic functions for temperature, and implicit Euler method for time discretization. The numerical code was extensively tested against the standard convection benchmark of *Blankenbach et al.* [1989].

4. Results

In this section, we describe the results of our study. Since we focus on the importance of thermal structure on the radar attenuation, we first describe the range of possible thermal states of Europa's ice shell (section 4.1) and then proceed with the description of the corresponding radar attenuations (section 4.2).

4.1. Thermal Structure of Europa's Ice Shell

The thermal state of Europa's ice shell (conductive or convective) depends largely on its viscosity structure and thickness which determine the critical Rayleigh number of the system [McKinnon, 1999; Barr and Pappalardo, 2005]. Unfortunately, no observations that would allow a robust estimate of the viscosity structure and the shell thickness are available. Various features observed at the surface may be compatible with a brittle-elastic lithosphere of few kilometers above a ductile and possibly convecting layer in the time of formation [e.g., *Pappalardo et al.*, 1999], but it is not clear whether the ice shell has remained in that state. Here we present a detailed overview of possible thermal states of Europa's shell for a wide range of model parameters (melting point viscosity η_0 , activation energy E_a , surface temperature T_s , magnitude of volumetric heating H_m , and shell thickness D). We are interested in the thermal regime (conductive, convective steady state, or convective chaotic) as well as the vertical and horizontal structures of the convecting shells (relative thickness of the conductive lid, number of convection cells, etc.). These properties are important to address since radar signal will be much less attenuated in the cold conductive lid and within the downwelling material at the convection cells' boundaries.

We start with the description of results for the reference set of parameters: $\eta_0 = 10^{14} \text{ Pa s}$, $E_a = 5 \times 10^4 \text{ J mol}^{-1}$, $T_s = 100 \text{ K}$, and negligible volumetric heating ($H_m = 0 \text{ W m}^{-3}$) while considering various shell thicknesses. Figure 1 depicts the temperature fields for $D = 5, 10, 15, 20, 25, 30 \text{ km}$ and shows that in thinner shells

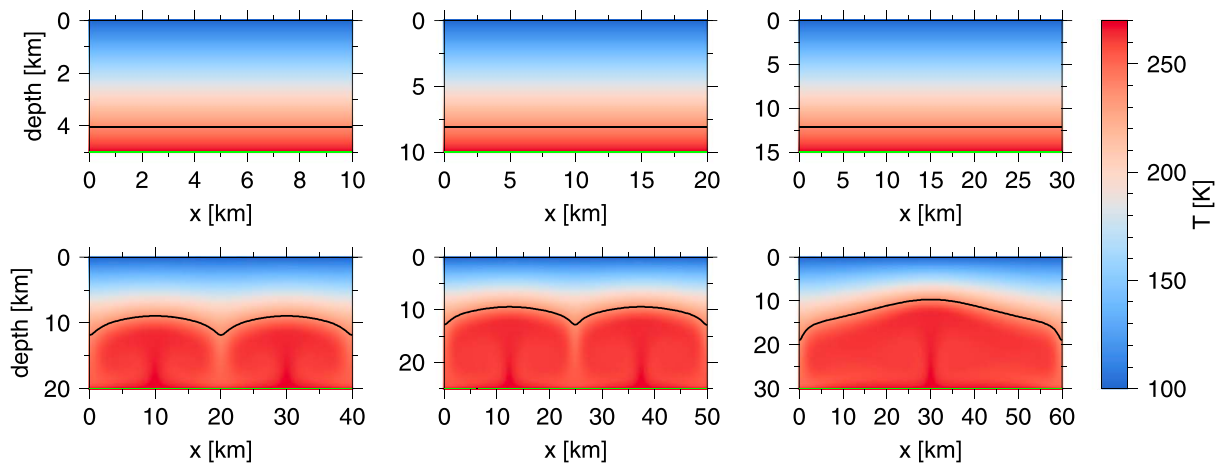


Figure 1. Temperature fields computed for $\eta_0 = 10^{14}$ Pa s, $E_a = 5 \times 10^4$ J mol $^{-1}$, $T_s = 100$ K, no volumetric heating $H_m = 0$ W m $^{-3}$, and different shell thicknesses $D = 5, 10, 15, 20, 25, 30$ km (from left to right and top to bottom). Black contour marks the eutectic temperature, $T = 237$ K; green contour marks the melting temperature of 270 K.

($D = 5–15$ km, top row), heat is transferred only by conduction, while in thicker shells ($D = 20–30$ km, bottom row) steady state convection occurs. In the convective cases, one or two convective cells are present depending on the shell thickness and, on average, the conductive lid constitutes about half of the shell. Melting temperature (270 K) is not reached anywhere in the domain (except for the bottom boundary where it is prescribed). The horizontally averaged temperature profiles corresponding to Figure 1 are shown in Figure 2e.

Varying the prescribed value of melting point viscosity η_0 significantly modifies the overall thermal structure of the shells (different columns of Figure 2). Decreasing the viscosity by 1 order of magnitude to 10^{13} Pa s (lower end-member for melting point viscosity) while keeping other model parameters as in the reference case (compare Figures 2d and 2e) results in convection occurring in shells 10 km or thicker; moreover, for $D \geq 20$ km, convection falls into the chaotic regime (in that case, simulations are run until a statistical steady state is achieved and attenuation is then evaluated from a random time instant). While in the steady state cases ($D = 10$ and 15 km), one or two convection cells are again formed, and the conductive lid forms about half of the layer; in the chaotic cases, the lateral structure varies in time and the relative thickness of the conductive lid gradually decreases with the increasing shell thickness to only about a quarter of the domain for $D = 30$ km. On the other hand, increasing the melting point viscosity by 1 order to 10^{15} Pa s (upper end-member for melting point viscosity, Figure 2f) leads to heat transfer only by conduction for all investigated shell thicknesses. Decreasing the surface temperature from 100 K that represents the average value for Europa to 50 K, which roughly corresponds to the minimum surface temperature, expected toward the poles [Ojakangas and Stevenson, 1989], while keeping the reference melting point viscosity $\eta_0 = 10^{14}$ Pa s (Figure 2e) results in 20 km thick shell being still conductive (while a 20 km shell with $T_s = 100$ K was convecting) and convection occurring in the steady state regime with two convective cells and conductive lid forming about 50% of the shell thickness for $D = 25$ and 30 km. Melting temperature was not reached in any of these simulations.

Now we investigate the effect of nonnegligible volumetric heating (compare Figures 2d–2f and 2g–2i) of the form given by equation (11) with $H_m = 5 \times 10^{-6}$ W m $^{-3}$ and $\eta_m = 1.5 \times 10^{14}$ Pa s [cf. Tobie *et al.*, 2003]. Starting again with the reference set of $\eta_0 = 10^{14}$ Pa s and $T_s = 100$ K (Figures 2e and 2h), we find that the conductive-convective transition occurs between shell thicknesses of 10 km (conductive) and 15 km (convective with two convection cells) instead of between 15 and 20 km as was the case when no volumetric heating was assumed. The conductive lid forms more than half of the domain for $D = 15$ km and decreases in relative thickness with the increasing shell thickness to slightly less than $\sim 50\%$ for $D = 30$ km. The fact that melting point viscosity of 10^{14} Pa s is very close to the viscosity that maximizes the volumetric heating (η_m) leads to almost maximal heating within the upwelling plumes (close/equal to melting point temperature) which further enhances the temperature increase and eventually ends by reaching the melting temperature within the convective portion of all convecting shells (the average temperature curve matches the melting point temperature curve in Figure 2h). We do not compute the amount of melt generated nor its effect on the shell dynamics; however, as reported by Tobie *et al.* [2003], the negative buoyancy of only a few percents of

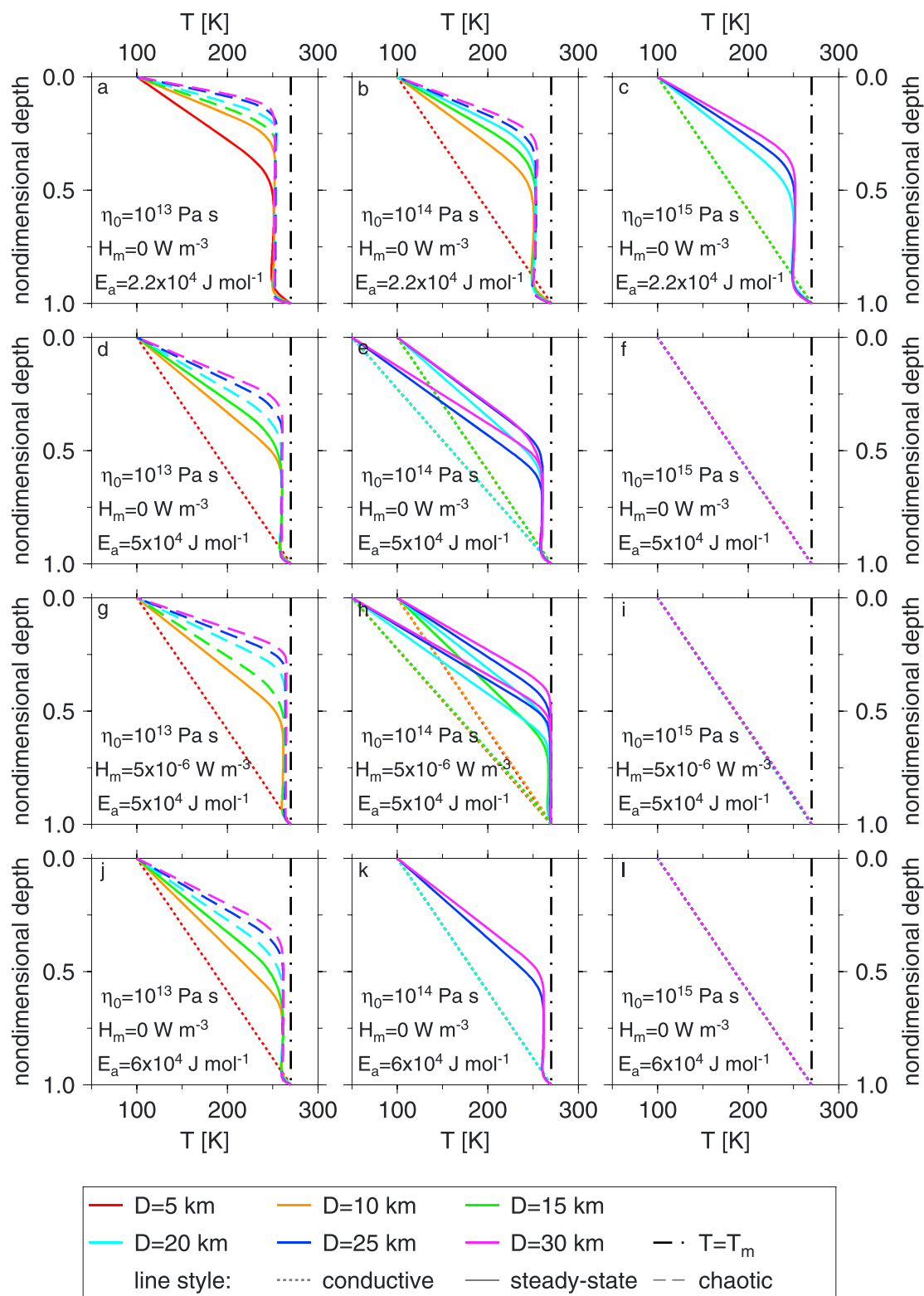


Figure 2. Horizontally averaged temperature profiles (depth is nondimensionalized) for all investigated cases. Colors represent the various shell thicknesses (5, 10, 15, 20, 25, and 30 km); line textures correspond to thermal regimes: conductive (dotted), convective steady state (solid), and convective chaotic (dashed). The black vertical dash-dotted line marks the melting temperature. Rows: Various activation energies and volumetric heating. Columns: Various melting point viscosities. Figures 2e and 2h also contain temperature profiles for simulations with $T_s = 50$ K.

water within the upwelling plumes would lead to a very rapid plume collapse thus significantly changing the thermal structure of the shell. We discuss the implications of omitting the melting processes in section 5.2. For $T_s = 50$ K, the conductive-convective transition again occurs for thinner shells (between 15 and 20 km) than when volumetric heating was not employed and melting temperature is reached within the convective portion of all convecting shells ($D \geq 20$ km).

In the case of different melting point viscosity η_0 , the effect of volumetric heating is much less pronounced. This is caused by the ratio of melting point and maximum heating viscosities, η_0/η_m , being very far from 1 which leads to the maximum heating occurring within the colder material (downwelling plumes and/or base of conductive lid; cf. Figure S5 in the supporting information) rather than in the upwelling warm plumes (cf. discussion by *Tobie et al.* [2003]). For $\eta_0 = 10^{13}$ Pa s (Figure 2g), the additional volumetric heating leads to chaotic convection for $D = 15$ km (instead of steady state as was the case with no volumetric heating) but otherwise the character of temperature field remains very similar with the conductive lid constituting about 25% (chaotic regime) up to ~50% (steady state regime) of the domain. Two convection cells are observed in the steady state regime ($D = 10$ km). For $\eta_0 = 10^{15}$ Pa s (Figure 2i), all investigated shells ($D = 5$ –30 km) are in conductive regime. In neither of these cases ($\eta_0 = 10^{13}$ and 10^{15} Pa s), melting temperature is reached, even though in the case of small melting point viscosity of 10^{13} Pa s, the convective portion of the shells is slightly warmer than in the case with no volumetric heating (compare Figures 2d and 2g).

Finally, we have investigated the effect of activation energy E_a (compare Figures 2a–2c and 2j–2l with Figures 2d–2f). Using the larger value, $E_a = 6 \times 10^4$ J mol $^{-1}$ (Figures 2j–2l), leads to about 3 orders of magnitude larger viscosity contrast across the shell with respect to the reference value of 5×10^4 J mol $^{-1}$, which in turn leads to less vigorous convection or conduction for certain shells that were in a convective regime for the reference value of activation energy. In the same sense, the lower bound for activation energy, $E_a = 2.2 \times 10^4$ J mol $^{-1}$ (Figures 2a–2c), causes some shells that were in conductive regime for the reference value of E_a to be convecting (compare Figures 2c and 2f) and similarly, increases the vigor of convection, leading to chaotic regime convection even for thinner shells (compare Figures 2a, 2d and 2b, 2e). In general, one or two convection cells are observed in the steady state cases with the conductive lid forming about half of the domain (with the exception of $E_a = 2.2 \times 10^4$ J mol $^{-1}$, $\eta_0 = 10^{13}$ Pa s, and $D = 10$ km, where the lid constitutes only about 25% of the domain), while in the chaotic cases, the horizontal structure becomes time variable with the conductive lid forming about 15% ($E_a = 2.2 \times 10^4$ J mol $^{-1}$, Figure 2a) to ~30% ($E_a = 6 \times 10^4$ J mol $^{-1}$, Figure 2j) of the shell.

To summarize, the critical thickness for the onset of convection strongly depends on the melting point viscosity as well as the activation energy—the smaller η_0 and/or E_a , the thinner the shell that can convect. The volumetric heating does not have a large effect on the onset of convection, although it can significantly increase the temperature of the convective portion of the shell for melting point viscosities of the order of 10^{14} Pa s and lead even to melting. For smaller or larger melting point viscosities, the effect of volumetric heating is less pronounced. Decreasing the surface temperature has a similar effect (although much less prominent) as increasing the activation energy and/or melting point viscosity, i.e., thicker shells are required for convection to occur. The 5 km thick shells were all found to be in conductive state for all investigated parameters (with the exception of 10^{13} Pa s and $E_a = 2.2 \times 10^4$ J mol $^{-1}$). On the other hand, the majority of shells with $D = 20$ km or thicker were found to be convecting (except for $\eta_0 = 10^{15}$ Pa s and $\eta_0 = 10^{14}$ Pa s and $T_s = 50$ K or $E_a = 6 \times 10^4$ J mol $^{-1}$).

The thermal states (conductive, convective steady state, or convective chaotic) of all investigated cases are indicated in Table 2. Figures of the type of Figure 1 for all investigated cases as well as volumetric heating for the cases with volumetric heating can be found in the supporting information. Let us note that our results are in reasonable agreement with the results of previous studies on the thermal state of the outer ice I shell of Europa inferred from scaling laws [*McKinnon*, 1999] as well as from numerical modeling [*Tobie et al.*, 2003; *Mitri and Showman*, 2005].

4.2. Radar Attenuation in Europa's Ice Shell

Here we evaluate the radar signal attenuation from the temperature fields described in the previous section. We again start with the description of results for our choice of reference model parameters ($\eta_0 = 10^{14}$ Pa s, $E_a = 5 \times 10^4$ J mol $^{-1}$, $T_s = 100$ K, and negligible volumetric heating, $H_m = 0$ W m $^{-3}$). Figure 3 shows the two-way attenuation corresponding to temperature fields from Figure 1 while considering the low loss ice model and

Table 2. Maximum (Cold Downwelling and Low Loss Ice, Left Number in Each Cell) and Minimum (Hot Upwelling and High Loss Ice, Right Number in Each Cell) Penetration Depths for Various Model Parameters (Melting Point Viscosities η_0 , Activation Energies E_a , Two Different Surface Temperatures T_s , Volumetric Heating Amplitudes H_m , and Shell Thicknesses D)^a

D	5 km		10 km		15 km		20 km		25 km		30 km	
$E_a = 5 \times 10^4 \text{ J mol}^{-1}, H_m = 0 \text{ W m}^{-3}$												
$\eta_0 = 10^{13} \text{ Pa s}, T_s = 100 \text{ K}$	5.0	5.0	10.0	6.0	15.0	6.3	17.0	6.8	16.0	7.8	14.1	7.8
$\eta_0 = 10^{14} \text{ Pa s}, T_s = 100 \text{ K}$	5.0	5.0	10.0	10.0	15.0	14.6	19.2	11.2	20.2	11.8	28.5	12.0
$\eta_0 = 10^{14} \text{ Pa s}, T_s = 50 \text{ K}$	5.0	5.0	10.0	10.0	15.0	14.8	20.0	19.4	24.0	14.8	25.2	15.6
$\eta_0 = 10^{15} \text{ Pa s}, T_s = 100 \text{ K}$	5.0	5.0	10.0	10.0	15.0	14.6	19.6	18.8	24.0	23.0	28.5	27.3
$E_a = 5 \times 10^4 \text{ J mol}^{-1}, H_m = 5 \times 10^{-6} \text{ W m}^{-3}$												
$\eta_0 = 10^{13} \text{ Pa s}, T_s = 100 \text{ K}$	5.0	5.0	10.0	5.8	14.6	6.0	12.0	6.4	12.8	6.5	12.0	6.6
$\eta_0 = 10^{14} \text{ Pa s}, T_s = 100 \text{ K}$	5.0	5.0	10.0	10.0	13.7	9.6	15.2	10.0	16.3	10.0	16.2	9.9
$\eta_0 = 10^{14} \text{ Pa s}, T_s = 50 \text{ K}$	5.0	5.0	10.0	10.0	15.0	14.7	15.8	12.2	17.3	12.8	19.2	13.2
$\eta_0 = 10^{15} \text{ Pa s}, T_s = 100 \text{ K}$	5.0	5.0	10.0	10.0	15.0	14.4	19.6	18.8	24.0	23.0	28.2	27.0
$E_a = 2.2 \times 10^4 \text{ J mol}^{-1}, H_m = 0 \text{ W m}^{-3}$												
$\eta_0 = 10^{13} \text{ Pa s}, T_s = 100 \text{ K}$	5.0	3.9	10.0	4.3	15.0	4.5	19.8	5.2	18.0	5.0	13.2	4.8
$\eta_0 = 10^{14} \text{ Pa s}, T_s = 100 \text{ K}$	5.0	5.0	10.0	6.0	15.0	6.0	20.0	6.2	25.0	6.8	27.0	7.5
$\eta_0 = 10^{15} \text{ Pa s}, T_s = 100 \text{ K}$	5.0	5.0	10.0	10.0	15.0	14.6	20.0	10.4	25.0	11.0	29.4	11.1
$E_a = 6 \times 10^4 \text{ J mol}^{-1}, H_m = 0 \text{ W m}^{-3}$												
$\eta_0 = 10^{13} \text{ Pa s}, T_s = 100 \text{ K}$	5.0	5.0	10.0	7.0	15.0	7.3	18.8	7.8	17.8	8.8	19.5	8.7
$\eta_0 = 10^{14} \text{ Pa s}, T_s = 100 \text{ K}$	5.0	5.0	10.0	10.0	15.0	14.6	19.6	18.8	21.2	13.8	22.5	14.1
$\eta_0 = 10^{15} \text{ Pa s}, T_s = 100 \text{ K}$	5.0	5.0	10.0	10.0	15.0	14.6	19.6	18.8	24.0	23.0	28.5	27.3

^aThe cell color corresponds to the relative penetration depth: cyan, ocean is reached; green, >75% of the shell thickness is penetrated; yellow, 50–75% of the shell thickness is penetrated; and red, <50% of the shell thickness is penetrated. The transition between thermal regimes (conductive/conductive steady state/conductive chaotic) is marked by thick lines with conductive regimes at bottom left and convective chaotic regimes at top right.

thus using equation (4) only with $i = 0$. The attenuation in the conductive cases in the top row ($D = 5, 10$, and 15 km) is very small in the large parts of shells. Taking 100 dB as the maximum two-way attenuation for which a subsurface return for a nominal satellite-borne radar sounder could be expected (cf. section 2), these shells can be penetrated all the way to the ocean. On the other hand, convection in the thicker shells ($20, 25$, and 30 km , bottom row) warms up large fractions of the individual shells leading to substantially larger attenuations and thus preventing whole shell radar signal penetration. However, the large lateral variability of the vertical attenuation profiles within the convecting shells indicates that much larger depths can be penetrated in the cold downwellings than on average as already suggested by McKinnon [2005]. To compare between particular cases in the next sections, we consider two distinct temperature profiles: (i) cold downwelling that is (in the steady state cases) located either in the middle of the computational domain or at the sides (cf. vertical cyan lines in Figure 3 (bottom row)) and is most favorable for radar penetration and (ii) the center of the upwelling plume (cf. vertical pink lines in Figure 3 (bottom row)), the worst for radar penetration. In the case of conductive shells, the temperature is laterally uniform and thus these two profiles coalesce and follow the conductive temperature profile. In the case of chaotic convection regime, the temperature profile is time variable which makes defining these profiles difficult. We thus choose a random time instant after the statistical steady state is reached and define the vertically averaged coldest and warmest profiles as the cold and hot profiles, respectively. We provide figures of the type of Figure 3 for all investigated cases and low loss ice model in the supporting information. We also provide the two-way attenuation evaluated for the reference case temperature fields (Figure 1) while assuming the high loss ice model (Figure S14 in the supporting information); however, the results are very similar to those obtained for the low loss ice model.

4.2.1. Attenuation Profiles—The Best- and Worst-Case Scenarios

We now investigate the effect of model parameters on the two-way attenuation. Figure 4 shows two-way attenuation evaluated for the cold temperature profiles (cf. above) as a function of depth and shell thickness

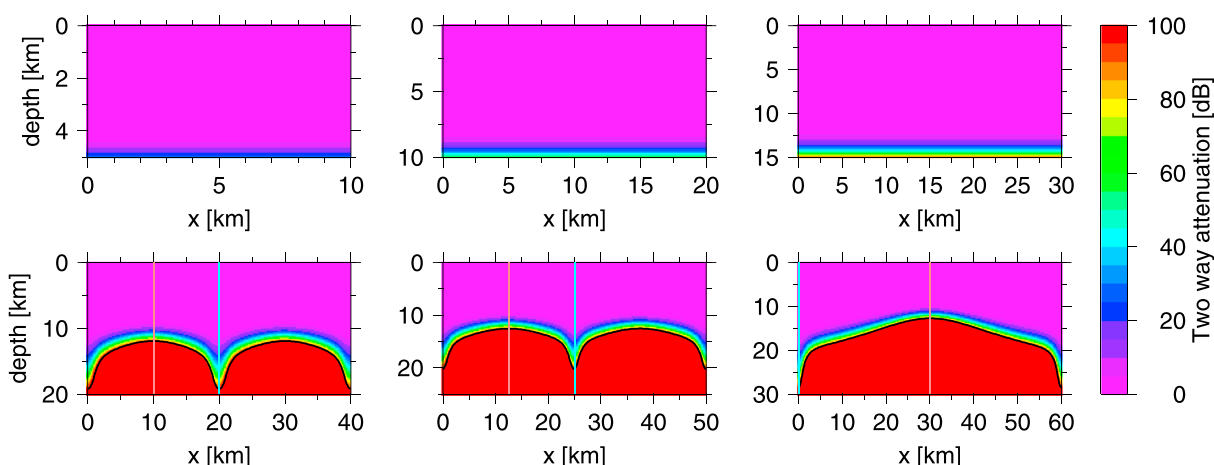


Figure 3. Two-way attenuation (considering low loss ice) corresponding to temperature fields from Figure 1 ($\eta_0 = 10^{14}$ Pa s, $E_a = 5 \times 10^4$ J mol $^{-1}$, and $T_s = 100$ K, no volumetric heating, and different shell thicknesses D). Black contour marks the attenuation of 100 dB. In the bottom row, the cyan and pink vertical lines mark the location of cold and hot profiles, respectively.

for various combinations of model parameters while considering only low loss ice model. For the smallest value of the melting point viscosity that was considered ($\eta_0 = 10^{13}$ Pa s, Figures 4a and 4b), only the thinnest investigated shell of 5 km is conductive with small attenuation, while convection starts for a relatively thin shell of only 10 km leading to warmer (and thus more attenuating) interior. For the shells of 15 km or more, attenuation values of ~ 100 dB are reached at depths around 15 km. Addition of volumetric heating (Figure 4b) results in attenuation of 100 dB being reached at depths of about 12–13 km in the convective shells, thus not changing the results significantly. This is likely caused by the fact that the maximum dissipation does not

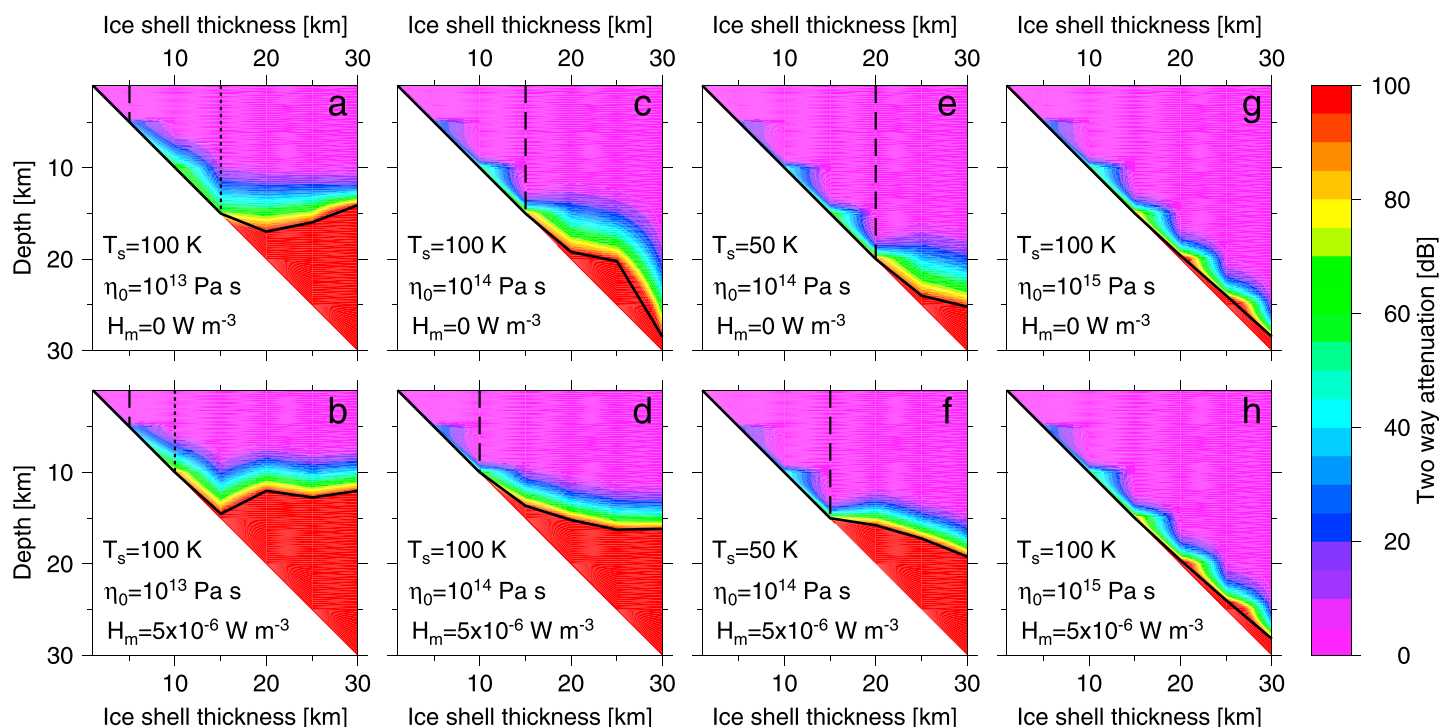


Figure 4. Two-way attenuation evaluated for the cold temperature profiles as a function of depth and shell thickness for various melting point viscosities η_0 , two different surface temperatures T_s , without (a, c, e, g) and with (b, d, f, h) volumetric heating, and considering low loss ice. The solid black lines denote the penetration depth (considering the value of 100 dB as an upper limit). Vertical lines mark the transition between conductive and convective steady state regimes (dashed) and convective steady state and convective chaotic regimes (dotted), respectively.

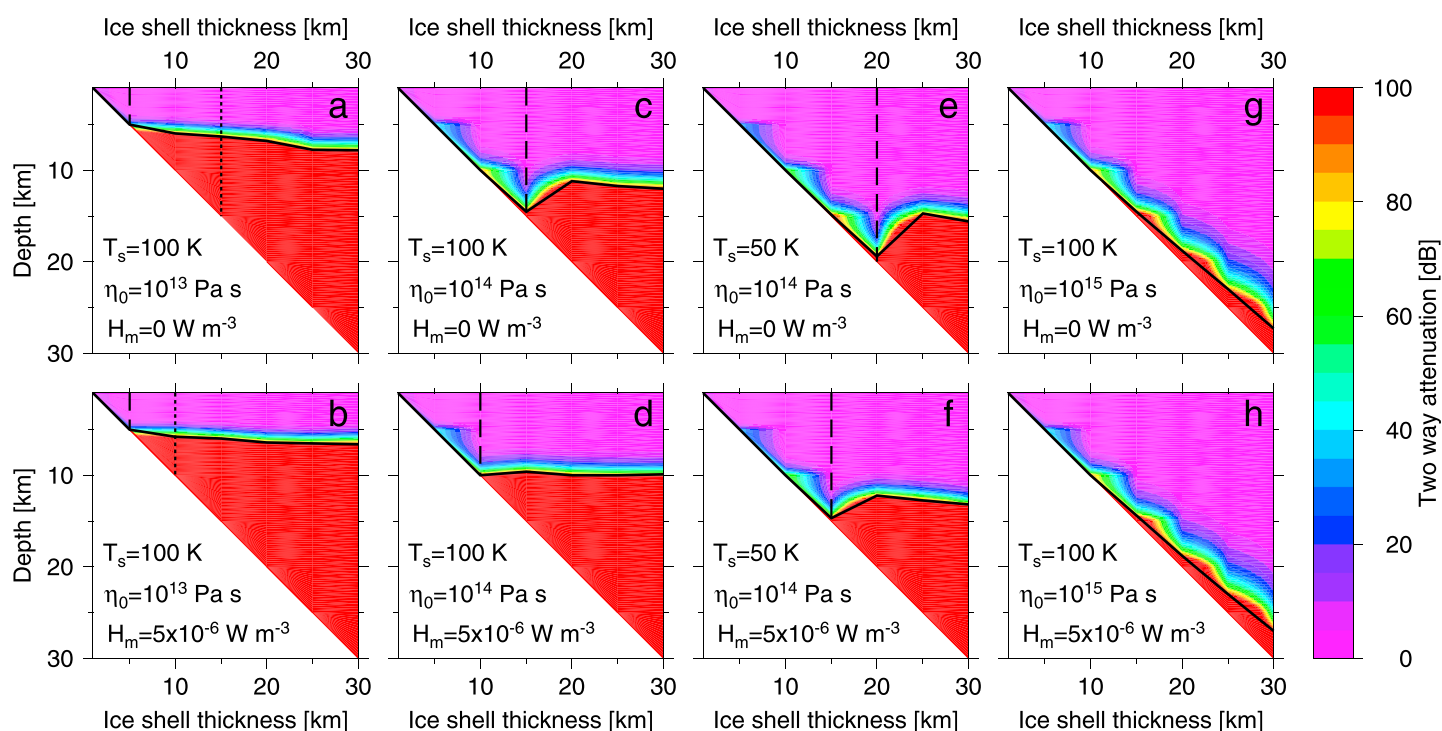


Figure 5. The same as in Figure 4 but for hot temperature profiles and high loss ice.

occur within the warm upwelling plumes but rather in the cold thermal boundary layer and/or within the downwelling cold plumes (cf. discussion on the effect of the ratio of η_m to η_0 in section 4.1).

For a larger melting point viscosity, $\eta_0 = 10^{14}$ Pa s, we have considered two values of surface temperature: $T_s = 100$ K (approximate average value) and $T_s = 50$ K (approximate polar value) [Ojakangas and Stevenson, 1989]. For $T_s = 100$ K and no volumetric heating (Figure 4c, the reference case, cf. also Figure 3), the attenuation is generally smaller than in the previous case (with $\eta_0 = 10^{13}$ Pa s and $T_s = 100$ K) and thus, within the thicker shells, attenuation of 100 dB is reached at depths of about 20 to 25 km. The addition of volumetric heating (Figure 4d) changes these results significantly by reducing the depth of 100 dB attenuation within the thicker shells to about 15 km. If smaller surface temperature is considered ($T_s = 50$ K, Figures 4e and 4f), attenuation limit of 100 dB is reached at slightly larger depths of ~ 25 km (for the case without volumetric heating, Figure 4e) and 15 to 20 km (for the case with volumetric heating, Figure 4f).

Finally, for the largest value of melting point viscosity considered in this study ($\eta_0 = 10^{15}$ Pa s, Figures 4g and 4h), the shell is conductive for all investigated thicknesses (up to 30 km) for both kind of simulations—with or without volumetric heating. The attenuation in the majority of the shell is thus much smaller than in the previous cases and only increases to 100 dB or more close to the bottom boundary.

The attenuation profiles depicted in Figure 4 represent the best-case scenarios for radar penetration since they are evaluated for the coldest temperature profile and considering the low loss attenuation model. To get the worst-case scenario, we consider the hot temperature profile and the high loss attenuation model—Figure 5 depicts the corresponding attenuations. Comparison of Figures 4 and 5 indicates that (i) in the conductive cases (left of vertical dashed lines and all investigated shell thicknesses for $\eta_0 = 10^{15}$ Pa s—Figures 5g and 5h), the difference between the best- and worst-case scenarios is small (given only by the chosen attenuation model since the temperature is laterally uniform in the whole shell) and with the exception of the thickest shells, the 100 dB attenuation limit is only reached very close to the bottom boundary or not reached at all in both scenarios (best and worse cases); (ii) in the convective cases (right of vertical dashed lines) the worst-case scenario leads to 100 dB attenuation at depths of only ~ 5 to 15 km, depending on the model parameters. We look on the values of 100 dB attenuation depths for both cases, best and worst, in more detail in the next section. Let us note that by giving the highest and lowest values, the realized penetration is likely to

fall between, even though we do not know the exact conditions in Europa's interior (temperature and chemistry) or the instrument (total attenuation depth that is most appropriate for a given instrument).

4.2.2. Local Penetration Depths

For the purpose of this study, we define the local penetration depth as a depth at which the 100 dB attenuation limit is reached—such local values of penetration depths will vary laterally in the convecting shell as opposed to a global single value considered in the majority of previous studies. We now employ both temperature profiles (cold and hot) and plot the corresponding local penetration depths as functions of the shell thickness in Figure 6 for the various model parameters investigated above and both attenuation models (cf. equation (4))—low loss ice (left column) and high loss ice (right column). We can summarize our findings into the following points: (i) only the thinnest shells with thicknesses ≤ 5 km could be penetrated all the way down to the ice/ocean interface for all investigated parameters, (ii) in the case of thicker shells (10–30 km), the melting point viscosity η_0 and the particular temperature profile are the key parameters in determining the penetration depth, with the surface temperature and amplitude of volumetric heating having second-order effects and the chosen attenuation model (high loss versus low loss) being of minor importance. For the largest value of the melting point viscosity ($\eta_0 = 10^{15}$ Pa s), all shells are conductive and so the majority of the shell ($\geq 90\%$) is penetrated for all shell thicknesses, not depending on the amplitude of volumetric heating and depending only negligibly on the attenuation model (low loss versus high loss ice). For the reference value, $\eta_0 = 10^{14}$ Pa s, the difference between penetration depths within the cold and hot profiles increases significantly: while in the cold profile (solid lines, best-case scenario), depths of up to 15 to ~ 25 km can be reached (especially when low loss ice attenuation model is considered), in the hot profile (dotted lines, worst-case scenario), the penetration depths are about 10 km (or more) smaller and do not exceed 15 km. The effect of the amplitude of tidal heating is also much more pronounced for $\eta_0 = 10^{14}$ Pa s, but the significant warming of large parts of the shells' interiors slightly reduces the difference between the cold and hot profiles with penetration depths of 10 (worst case) to ~ 15 km (best case). Decreasing the surface temperature leads to slightly larger penetration depths of about 20 to 25 km (cold profile) and 15 to 20 km (hot profile) in the case without volumetric heating and 13 to ~ 19 km in the case with volumetric heating (here again, the volumetric heating suppresses the difference between cold and hot profiles). In the case of the smallest melting point viscosity, $\eta_0 = 10^{13}$ Pa s, the smallest portions of the shells can be penetrated and the difference between cold and hot profile penetration depths is the largest (especially when there is no volumetric heating)—in the cold profiles, penetration depths are found to be roughly between 10 and 15 km, depending on the total shell thickness, amplitude of heating, and attenuation model, while in the hot profiles, depths of only about 5 to 8 km can be reached (almost independently on the amplitude of volumetric heating, attenuation model, and shell thickness).

Finally, we also investigated the effect of the activation energy E_a by considering two different values of 2.2×10^4 and 6×10^4 J mol $^{-1}$ (that roughly correspond to the envelope of activation energies for various creep mechanisms) [e.g., *Showman and Han, 2005*]. Figure 7 shows the penetration depths for these two activation energies, the same melting point viscosities as above (10^{13} – 10^{15} Pa s), no volumetric heating ($H_m = 0$ W m $^{-3}$), both temperature profiles (cold and hot), and both attenuation models (low loss, high loss ice). Even though varying the activation energies affects the results of numerical simulations, the penetration depths are not significantly different from the reference case ($E_a = 5 \times 10^4$ J mol $^{-1}$): Shells up to about 15 km thick can be penetrated to the ocean for all viscosities—either if the shell is conductive ($\eta_0 = 10^{15}$ Pa s) or within the cold downwelling ($\eta_0 = 10^{13}$ – 10^{14} Pa s). In the case of thicker shells, the penetration depth depends mainly on the melting point viscosity η_0 and the temperature profile. For the smallest value, 10^{13} Pa s, depths of 10 to 20 km (cold profile) and 5 to 10 km (hot profile) can be reached, while for 10^{14} Pa s, depths of about 20 to 25 km (cold profile) and 5 to 10 km (hot profile, $E_a = 2.2 \times 10^4$ J mol $^{-1}$) or 15 to 20 km (hot profile, $E_a = 6 \times 10^4$ J mol $^{-1}$) can be penetrated and for 10^{15} Pa s, almost the whole shell is penetrated ($E_a = 6 \times 10^4$ J mol $^{-1}$ or cold profile for $E_a = 2.2 \times 10^4$ J mol $^{-1}$) or depths of ~ 10 to 15 km are reached (hot profile and $E_a = 2.2 \times 10^4$ J mol $^{-1}$).

In general, our results indicate that (i) the ice/ocean interface can be always detected by a radar sounder if the shell is about 5 km thick or thinner for almost all investigated cases; (ii) might be detected if the shell is 10 to 15 km thick (or up to ~ 25 km in the case of very low activation energy), the radar signal travels through a cold downwelling and the ice is not much attenuating; and (iii) cannot be detected (i.e., the two-way attenuation is > 100 dB) if the shell is more than ~ 20 km thick. However, in these thicker shells, the penetration depth still varies significantly (depending mainly on the viscosity, amplitude of heating, and temperature profile), and even if the ice/ocean interface is not reached, the penetration through most of the shell (especially for $\eta_0 = 10^{15}$ Pa s) could allow detection of deep structures (e.g., potentially accreted ice) and help

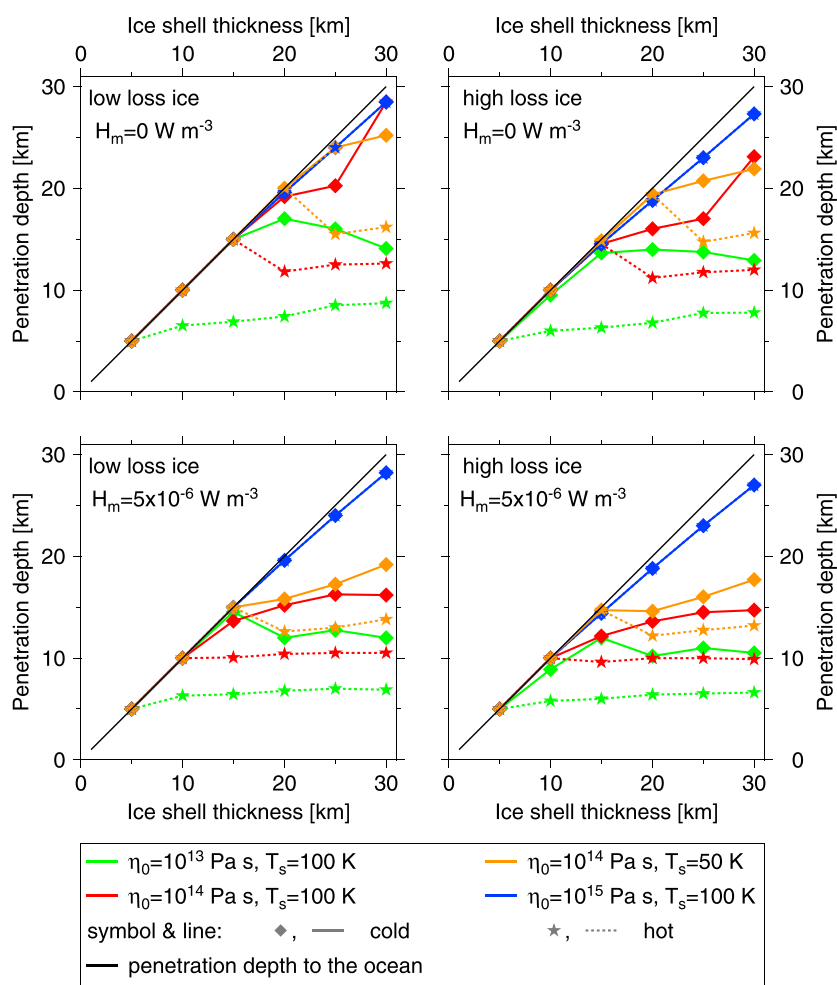


Figure 6. Penetration depth as a function of the shell thickness for various melting point viscosities η_0 , two different surface temperatures T_s , without (top row) and with (bottom row) volumetric heating, and considering low loss ice (left column) as well as high loss ice (right column). Black lines mark the penetration depth to the ocean. Different symbols and line styles correspond to different temperature profiles: cold (diamond, solid line) and hot (asterisk, dotted line).

constrain the attenuation rates through the loss of signal. Also, the observed radar signal pattern might help determine the thermal (conductive/convective) state of the shell through the comparison with the results of numerical modeling. We provide the maximum (cold profile, low loss ice) and minimum (hot profile, high loss ice) penetration depths for all investigated parameters together with the thermal regimes in Table 2. Let us note that we have also evaluated the local penetration depths for the horizontally averaged temperature profiles from Figure 2—these are, in general, similar to those obtained for the hot profiles, but about few kilometers larger, and are not depicted in Figures 6 and 7 for the sake of clarity.

4.2.3. Comparison With Previous Studies

As already mentioned in section 1, several authors have so far addressed the attenuation within Europa's shell. In their studies, Chyba *et al.* [1998], Moore [2000], and Blankenship *et al.* [2009] all reported similar ice/ocean interface detectability limits of about 10 km corresponding to a conductive shell. For thicker convective shells, they found that the radar sounder would not be able to detect the deep ice/ocean interface. However, as first indicated by McKinnon [2005] and later investigated by Di Paolo *et al.* [2014], in the convective shells, the penetration depth strongly varies laterally with the deepest penetration possible through the cold downwellings. Recently, Di Paolo *et al.* [2016] performed a numerical study to address this effect using an approach similar to ours, however, while investigating smaller parameter space (in terms of ice viscosity and tidal heating parametrization). Their results can be compared with our results for $E_a = 6 \times 10^4 \text{ J mol}^{-1}$ and $\eta_0 = 10^{13} - 10^{14} \text{ Pa s}$: (i) for the conductive shell ($\eta_0 = 10^{14} \text{ Pa s}$), Di Paolo *et al.* [2016] report ocean detection

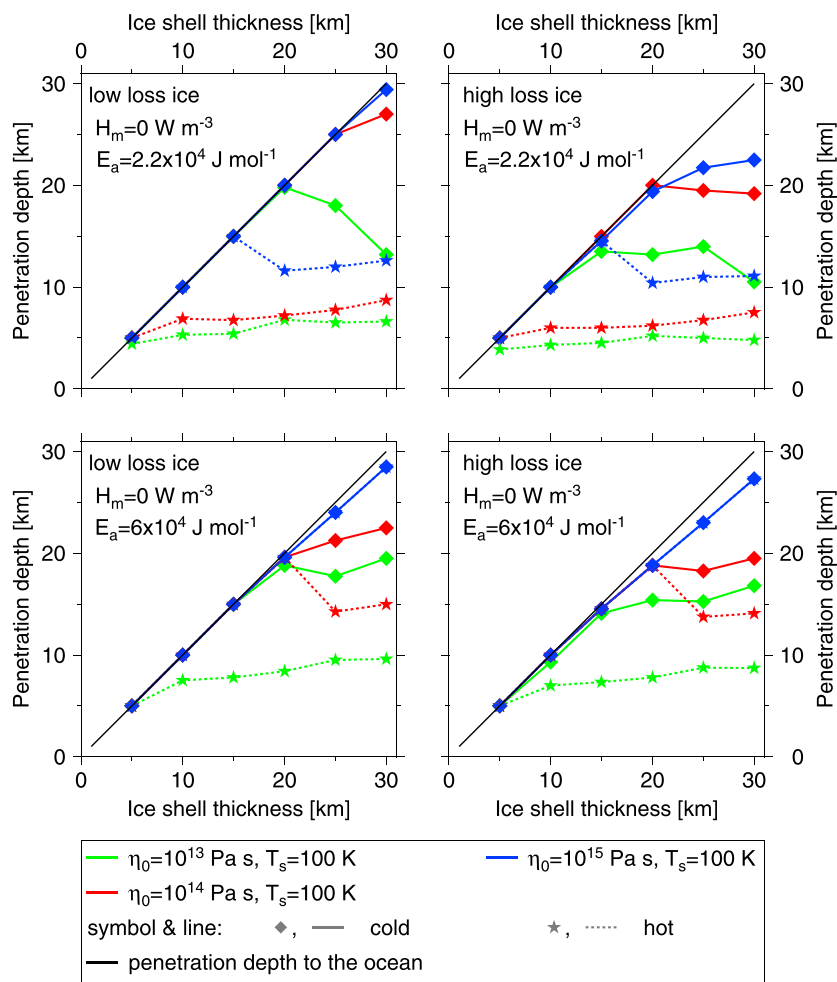


Figure 7. The same as in Figure 6 but for $E_a = 2.2 \times 10^4 \text{ J mol}^{-1}$ (top row) and $6 \times 10^4 \text{ J mol}^{-1}$ (bottom row).

depth of about 15 km that is in agreement with our results for low loss ice and (ii) for the convective shell ($\eta_0 = 10^{13} \text{ Pa s}$) they report the ocean detection depth of 12 km which is only slightly smaller than our value of 15 km (cf. also Table 2). In general, our results agree well with the previously published studies and extend their validity by investigating a broader range of material/physical parameters.

4.2.4. Attenuation to the Eutectic Temperature

Interstitial brines and/or brine pockets might form within the ice shell where temperature exceeds the eutectic isotherm. This onset of melting will cause a significant transition in dielectric properties, and the brines will act as a strong signal reflector [e.g., Dowdeswell and Evans, 2004] thus generating a pervasive reflection signal at the eutectic isotherm. Mapping the distribution of these brines might provide additional information on the ice shell's thermal structure.

The eutectic isotherm depends on the composition of the ice shell and, particularly, on the type of salt dissolved (i.e., sulfate rich or chloride rich) [Kargel et al., 2000]. Here we assume the K_{1a} European ocean composition model of Zolotov and Shock [2001], which optimizes the Mg-Ca-Na-K-Cl-S-H₂O system for European chemistry using the FREZCHEM code [Marion and Grant, 1994; Mironenko et al., 1997] and forms magnesium and sodium hydrous sulfates most abundantly with complete freezing occurring below 237 K. If, alternatively, the ice shell is more rich in hydrated chloride salts, the eutectic temperature is in the range of 220–250 K [Richardson, 1976]. Thus, $T_{\text{eut}} = 237 \text{ K}$ is a reasonable estimate for either composition. Let us note that the partial melting is assumed to be caused by the presence of a relatively small amount of salt within the cold lid. Due to this assumption, we can neglect the effect of salts on the shell dynamics (cf. also section 5.3).

Figure 8 shows the two-way attenuations to reach the eutectic temperature as a function of lateral coordinate (x) for the same set of simulations as in Figure 6 and for the thickest shell considered (30 km). In the case of low

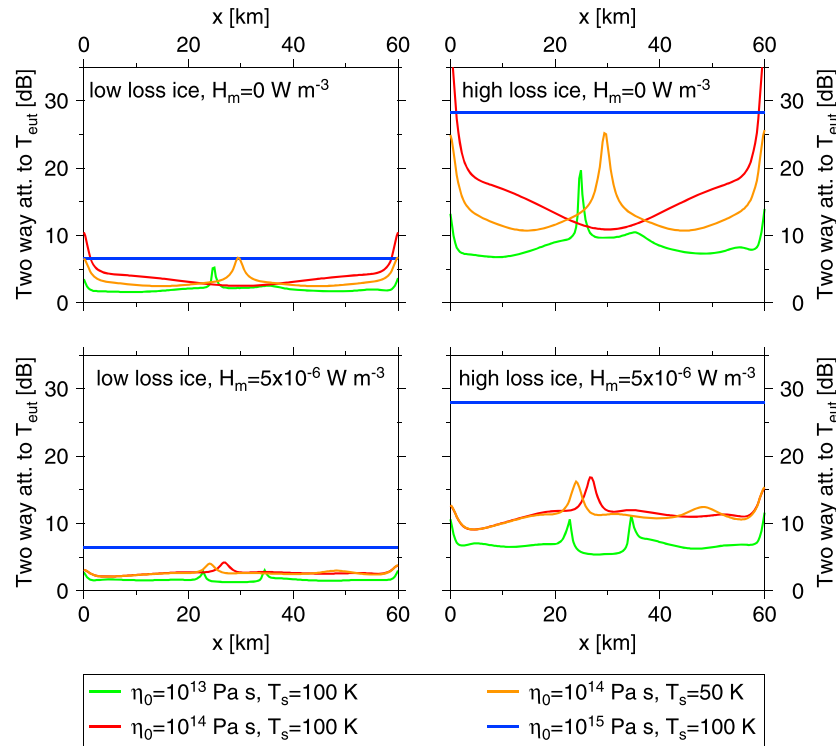


Figure 8. Two-way attenuation to the eutectic temperature ($T_{\text{eut}} = 237$ K) for 30 km thick shell as a function of horizontal coordinate for various melting point viscosities η_0 , two different surface temperatures T_s , without (top row) and with (bottom row) volumetric heating, and considering low loss ice (left column) as well as high loss ice (right column).

loss ice (left column), the attenuation rates are smaller than 10 dB for all investigated cases, while in the case of high loss ice (right column), the attenuation rates vary between ~ 8 and 30 dB with the largest values found for the largest viscosities (conductive shells) or in the cold downwellings (convective shells) where the isotherm is located deeper in the ice shell and the smallest values corresponding to the top of hot upwelling plumes. The particular choice of attenuation model (low loss versus high loss) also plays a significant role—the attenuation to reach the eutectic temperature increases more than two times when we consider high loss instead of low loss ice (i.e., by moving from Figure 8, left column to Figure 8, right column). For smaller shell thicknesses, the attenuation rates to reach the eutectic temperature are even smaller. In general, the warmer the interior (smaller viscosity, larger volumetric heating), the smaller the attenuation to reach the eutectic point. The depths of the eutectic isotherm vary accordingly from approximately 5 km to about 15 km on average, with smaller values (2 km) found for the simulations with the smallest value of activation energy (2.2×10^4 J mol $^{-1}$) and the largest values (up to ~ 25 km) found for the simulations with the largest value of melting point viscosity (10^{15} Pa s). Overall, our results suggest that there should be a lot of additional signal available for detecting the shallow brine pockets (if they are present) as well as reflection from the potential global dielectric transition at the eutectic point itself.

5. Discussion

We now discuss some of the model assumptions and their effect on the obtained results.

5.1. Temperature-Dependent Thermal Conductivity

In this study, we have so far considered a constant value of thermal conductivity ($k = 2.28$ W m $^{-1}$ K $^{-1}$) throughout the shell. However, the temperature dependence of this material parameter might significantly change our results since it influences the shell's thermal structure. To investigate this effect, we have designed an additional set of simulations for the reference values of parameters ($\eta_0 = 10^{14}$ Pa s, $E_a = 5 \times 10^4$ J mol $^{-1}$, and $T_s = 100$ K) where we considered a temperature dependence of thermal conductivity of the form:

$$k(T) = \frac{k_1}{T} + k_2, \quad (12)$$

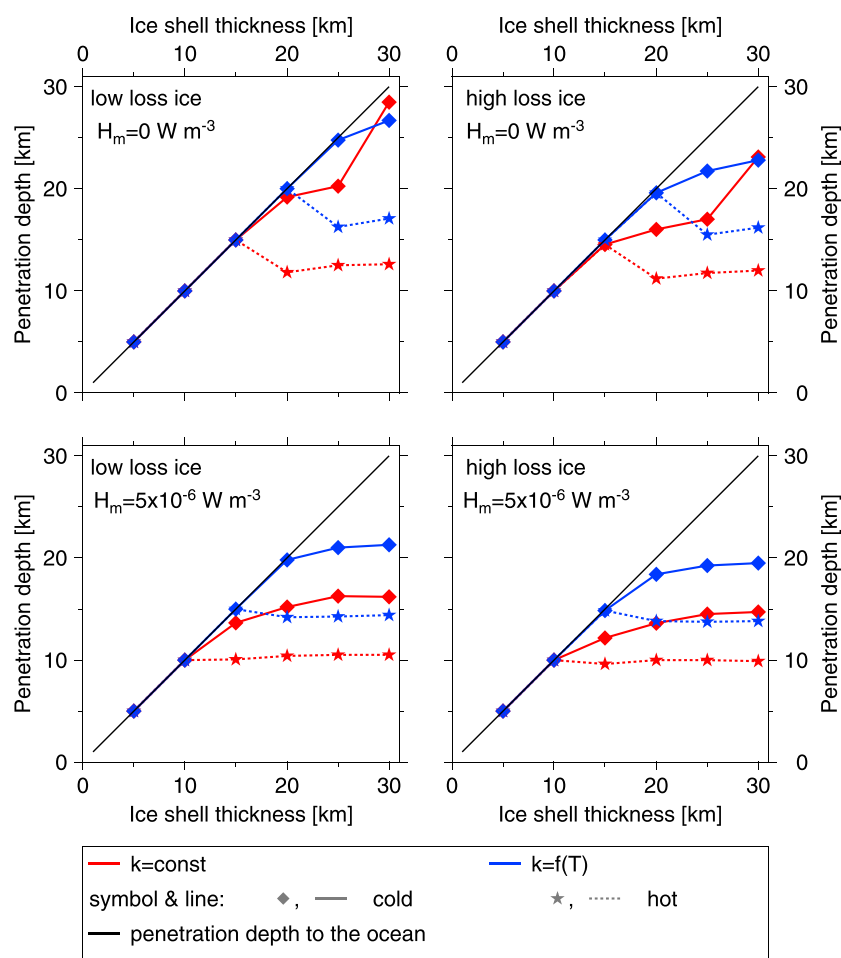


Figure 9. Penetration depth as a function of the shell thickness for $\eta_0 = 10^{14} \text{ Pa s}$, $E_a = 5 \times 10^4 \text{ J mol}^{-1}$, $T_s = 100 \text{ K}$, $H_m = 0 \times 10^{-6} \text{ W m}^{-3}$ (top row) or $H_m = 5 \times 10^{-6} \text{ W m}^{-3}$ (bottom row), low loss ice (left column) versus high loss ice (right column), and $k = \text{const}$ (red) versus $k = f(T)$ (blue). Different symbols and line styles correspond to different temperature profiles: cold (diamond, solid line) and hot (asterisk, dotted line). Black lines mark the penetration depth to the ocean.

with $k_1 = 488.12 \text{ W m}^{-1}$ and $k_2 = 0.4685 \text{ W m}^{-1} \text{ K}^{-1}$ [Hobbs, 1974], resulting in $k = 2.28$ and $5.35 \text{ W m}^{-1} \text{ K}^{-1}$ at the bottom and surface of the shell, respectively. We have again considered the same shell thicknesses ($D = 5, 10, 15, 20, 25$, and 30 km) and the same heating rate amplitudes ($H_m = 0$ and $5 \times 10^{-6} \text{ W m}^{-3}$). We provide several figures depicting results of these simulations in the supporting information: Figures S15 and S16 show temperature, heating rate (for simulations where it was nonzero), and two-way attenuation (considering low loss ice); Figure S17 shows comparison of horizontally averaged temperature profiles for the cases with constant and temperature-dependent thermal conductivity, respectively; and Figure S18 shows comparison of two-way attenuation as a function of depth and shell thickness for the same set of simulations. Finally, Figure 9 shows comparison of penetration depths for these simulations. Our results indicate that (i) when temperature dependence of thermal conductivity of the form (12) is taken into account, convection starts for slightly thicker shells than in the case with $k = \text{const}$, (ii) in the convective shells, the conductive lid is slightly thicker if temperature-dependent conductivity is considered, (iii) penetration depths are about 5 km larger in the case of variable thermal conductivity (cf. also Table S1 in supporting information). Overall, the effect of temperature-dependent thermal conductivity is very similar to that of decreasing the surface temperature T_s to 50 K . We conclude that, even though the effect of temperature-dependent thermal conductivity is not negligible, the newly obtained results, in terms of thermal regimes as well as penetration depths, fall well within the range of results obtained with constant thermal conductivity and different viscosity parametrizations (activation energy E_a and melting point viscosity η_0) and/or surface temperatures T_s .

5.2. Neglect of Melting

In some simulations where volumetric tidal heating of the form given by equation (11) was considered, the melting temperature was reached within the convective part of the shell. We did not compute the amount of generated melt nor considered its effect on the shell dynamics, but we merely fixed the temperature on the melting point even though the presence of liquid water (more dense than ice I) would very likely influence the temperature evolution. However, any meltwater generated within the convective part of the shell would be transported toward the underlying ocean on short timescales—either by porous extraction through the warm ice that is at the melting temperature [Kalousová *et al.*, 2014] or by solid-state convection [Tobie *et al.*, 2003; Kalousová *et al.*, 2016] if the ice below the generated liquid is cold (below melting temperature) and the water stays trapped within the solid ice. In both cases (porous flow and solid-state convection), the thermal structure, which is the most important parameter controlling the radar signal attenuation in our application, would not change dramatically (e.g., convective shell would not become conductive, etc.). We thus believe that the presence of a few percents of interstitial meltwater within the convective part of the shell would not significantly affect the radar signal attenuation.

5.3. Composition

Spectroscopic observations of Europa's disrupted surface areas suggest the presence of salts within the ice shell [e.g., McCord *et al.*, 1998; Kargel *et al.*, 2000; Zolotov and Kargel, 2009] that might lower the melting temperature by several tens of Kelvins [e.g., Kargel *et al.*, 2000; Pappalardo and Barr, 2004]. If the contaminants are predominantly located in the upper part of the ice shell, concentrated brines might form at shallow depths that would cause a significant transition in dielectric properties and reflect the radar signal. To estimate the effect of salty constituents on the radar performance, we considered the high loss attenuation model, but we neglected the effect of salts on the shell dynamics (by solving the problem of thermal as opposed to thermochemical convection). As we have shown in section 4.2.4, the shallow subsurface brines should be detectable by radar sounding—their global mapping might bring a valuable insight about the shell properties (thickness, viscosity, and composition) and its thermal regime. Further modeling efforts are, however, needed to quantify more precisely the role of low-eutectic constituents.

5.4. Linear Rheology

Our results indicate that the actual viscosity value (parametrized here through values of η_0 and E_a) has a large effect on the thermal structure and thus on the attenuation within the ice shell. Even though ice viscosity is a highly nonlinear function of temperature, pressure, stress, grain size, and water content, we have considered only its temperature dependence (equation (10)). To cover the possible range of thermal states of Europa's ice shell, we have varied the values of melting point viscosity η_0 (roughly corresponding to variations in grain size) and activation energy E_a (mimicking different deformation mechanisms). Also, the brittle-ductile transition (not considered in this study but expected to occur at depth of 1–2 km) [e.g., Pappalardo *et al.*, 1999] would effectively reduce the viscosity contrast across the shell, possibly resulting in thinner conductive lid and smaller penetration depths. A proper treatment of plastic rheology (a continuum representation of brittle behavior) is well beyond the scope of this study but might be considered in a following work.

5.5. Aspect Ratio and Mechanical Boundary Conditions

We have performed all simulations in a Cartesian box with aspect ratio $\lambda = 2$ and the free slip condition prescribed at all boundaries. The choice of this narrow box might affect our results since the box size controls the geometry of the convective interior. To quantify this effect, we have performed additional simulations, in which we considered the reference values of parameters ($\eta_0 = 10^{14}$ Pa s, $E_a = 5 \times 10^4$ J mol⁻¹, $T_s = 100$ K, and Table 1) but different boundary conditions or domain aspect ratio. The first set of simulations (for shell thicknesses between 5 and 30 km) is computed in the same box with aspect ratio $\lambda = 2$ but with the periodic boundary condition on the sides (simulations R1), while the other two sets are performed for domains with aspect ratios $\lambda = 3$ (simulations R2) and $\lambda = 6$ (simulations R3), respectively, and with free slip conditions on side boundaries. We plot the results of these simulations in the supporting information: Figures S19–S21 show temperature and two-way attenuation (considering low loss ice); Figure S22 shows comparison of the horizontally averaged temperature profiles evaluated from the results of the new simulations (R1–R3) with those evaluated for the reference case, and Figure S23 shows comparison of the two-way attenuation as a function of depth and shell thickness for the same set of simulations. Finally, Figure 10 shows comparison of the penetration depths for these simulations. Our results indicate that the effect of different aspect ratio

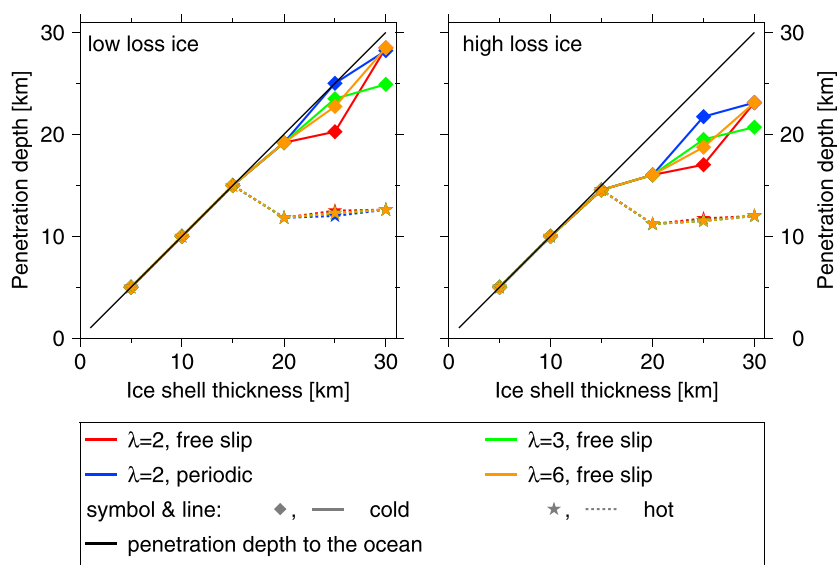


Figure 10. Penetration depth as a function of the shell thickness for $\eta_0 = 10^{14}$ Pa s, $E_a = 5 \times 10^4$ J mol $^{-1}$, $T_s = 100$ K, and $H_m = 0 \times 10^{-6}$ W m $^{-3}$ and considering low loss ice (left column) and high loss ice (right column). Reference simulation (red) compared with the simulations R1 (blue), R2 (green), and R3 (yellow). Different symbols and line styles correspond to different temperature profiles: cold (diamond, solid line) and hot (asterisk, dotted line). Black lines mark the penetration depth to the ocean.

(or periodic boundary condition), in terms of the shell's thermal state as well as in terms of maximal and minimal penetration depths (cf. also Table S2 in supporting information), is negligible when compared to the effect of viscosity parameterization represented by the choice of E_a and η_0 .

6. Conclusions

In the present study, we investigated the two-way attenuation within the icy shell of Europa in order to constrain the performance of future satellite-borne ice-penetrating radars. First, we solved the solid-state thermal convection equations for a broad range of model parameters (melting point viscosity, activation energy, surface temperature, amplitude of volumetric heating, and shell thickness) in order to obtain an envelope of possible thermal states of Europa's shell. Second, we assumed that the propagation of radar signal depends solely on the temperature structure, and we evaluated the two-way attenuation within the shell for two models—low loss ice (corresponding to pure ice with no impurities) and high loss ice (corresponding to ice containing some amount of salts and acids).

Our results indicate that (i) for all ice shell thicknesses investigated (5–30 km), a nominal satellite-borne radar sounder will penetrate between 15% and 100% of the total thickness (varying with the model parameters), which corresponds to maximum signal detection depths from 5 to ~29 km, (ii) in the convective shells, the maximum penetration depth strongly varies laterally, with the deepest penetration possible through the cold downwellings, (iii) the direct detection of the ice/ocean interface might be possible for shells of up to ~15 km thick (or ~25 km in the case of very low activation energy) if the radar signal travels through a cold downwelling (or the shell is conductive), (iv) even if the ice/ocean interface is not directly detected, the penetration through most of the shell (especially if viscosity is large) could constrain the deep shell structure through the loss of signal, and (v) for all plausible ice shells, the two-way attenuation to the eutectic point is $\lesssim 30$ dB which shows a robust potential for longitudinal investigation of the shallow structure of the ice shell.

Overall, we have demonstrated that future spacecraft exploration of Europa's ice shell by radar sounding has a strong potential to unveil important characteristics of its thermophysical structure, which can place constraints on the thickness by revealing the geometry of convection, and possibly also to directly detect the ice/ocean interface.

Acknowledgments

The authors would like to thank three anonymous reviewers and both editors for their valuable comments that helped to improve the quality of the manuscript. Part of this work was carried out at the Jet Propulsion Laboratory, California Institute of Technology, under a contract with the National Aeronautics and Space Administration. K.K. acknowledges support by the office of the JPL Chief Scientist. K.M.S. acknowledges support from NASA grant NNX14AR28G. This research received funding from the Czech Science Foundation through project 15-14263Y (K.K.) and was also supported by the IT4Innovations Centre of Excellence project (CZ.1.05/1.1.00/02.0070). The data produced by the numerical model are available at <http://geo.mff.cuni.cz/~kalous/radar/data.tar.gz>.

References

- Aglyamov, Y., D. M. Schroeder, and S. D. Vance (2017), Bright prospects for radar detection of Europa's ocean, *Icarus*, 281(1), 334–337, doi:10.1016/j.icarus.2016.08.014.
- Alnæs, M., J. Blechta, J. Hake, A. Johansson, B. Kehlet, A. Logg, C. Richardson, J. Ring, M. E. Rognes, and G. N. Wells (2015), Supporting computer code for 'The FEniCS Project Version 1.5' (release notes), *Arch. Numer. Softw.*, 3(100), 9–23.
- Anderson, J. D., G. Schubert, R. A. Jacobson, E. L. Lau, W. B. Moore, and W. L. Sjogren (1998), Europa's differentiated internal structure: Inferences from four Galileo encounters, *Science*, 281(5385), 2019–2022, doi:10.1126/science.281.5385.2019.
- Barr, A. C., and R. T. Pappalardo (2005), Onset of convection in the icy Galilean satellites: Influence of rheology, *J. Geophys. Res.*, 110(E12005), doi:10.1029/2004JE002371.
- Běhounková, M., G. Tobie, G. Choblet, and O. Čadež (2012), Tidally-induced melting events as the origin of south-pole activity on Enceladus, *Icarus*, 219(2), 655–664, doi:10.1016/j.icarus.2012.03.024.
- Bierhaus, E. B., K. Zahnle, and C. R. Chapman (2009), Europa's crater distributions and surface ages, in *Europa*, edited by R. T. Pappalardo, W. B. McKinnon, and K. Khurana, pp. 161–180, Univ. of Ariz. Press, Tucson.
- Bingham, R. G., and M. J. Siegert (2007), Radio-echo sounding over polar ice masses, *J. Environ. Eng. Geoph.*, 12(1), 47–62, doi:10.2113/JEEG12.1.47.
- Billings, S. E., and S. A. Kattenhorn (2005), The great thickness debate: Ice shell thickness models for Europa and comparisons with estimates based on flexure at ridges, *Icarus*, 177(2), 397–412, doi:10.1016/j.icarus.2005.03.013.
- Blankenbach, B., et al. (1989), A benchmark comparison for mantle convection codes, *Geophys. J. Int.*, 98(1), 23–38, doi:10.1111/j.1365-246X.1989.tb05511.x.
- Blankenship, D. D., D. A. Young, W. B. Moore, and J. C. Moore (2009), Radar sounding of Europa's subsurface properties and processes: The view from Earth, in *Europa*, edited by R. T. Pappalardo, W. B. McKinnon, and K. Khurana, pp. 631–654, Univ. of Ariz. Press, Tucson.
- Brown, M. E., and K. P. Hand (2013), Salts and radiation products on the surface of Europa, *Astron. J.*, 145(4), 110, doi:10.1088/0004-6256/145/4/110.
- Bruzzzone, L., et al. (2015), Jupiter Icy Moons Explorer (JUICE): Advances in the Design of the Radar for Icy Moons (RIME), in *Proceedings of the 35th IEEE International Geoscience and Remote Sensing Symposium (IGARSS 2015)*, pp. 1257–1260, Milan, Italy, doi:10.1109/IGARSS.2015.7326002.
- Carlson, R. W., R. E. Johnson, and M. S. Anderson (1999), Sulfuric acid on Europa and the radiolytic sulfur cycle, *Science*, 286(5437), 97–99, doi:10.1126/science.286.5437.97.
- Carr, M. H., et al. (1998), Evidence for a subsurface ocean on Europa, *Nature*, 391(6665), 363–365, doi:10.1038/34857.
- Chyba, C. F., S. J. Ostro, and B. C. Edwards (1998), Radar detectability of a subsurface ocean on Europa, *Icarus*, 134(2), 292–302, doi:10.1006/icar.1998.5961.
- Collins, G., and F. Nimmo (2009), Chaotic terrain on Europa, in *Europa*, edited by R. T. Pappalardo, W. B. McKinnon, and K. Khurana, pp. 259–281, The Univ. of Ariz. Press, Tucson.
- Corr, H., J. C. Moore, and K. W. Nicholls (1993), Radar absorption due to impurities in Antarctic ice, *Geophys. Res. Lett.*, 20(11), 1071–1074, doi:10.1029/93GL01395.
- De La Chapelle, S., H. Milsch, O. Castelnau, and P. Duval (1999), Compressive creep of ice containing a liquid intergranular phase: Rate-controlling processes in the dislocation creep regime, *Geophys. Res. Lett.*, 26(2), 251–254, doi:10.1029/1998GL000289.
- Di Paolo, F., B. Cosciotti, S. E. Lauro, E. Mattei, E. Pettinelli, and G. Vannaroni (2014), Thermal and electromagnetic models for radar sounding of the Galilean satellite icy crusts, in *Proceedings of the 15th International Conference on Ground Penetrating Radar, GPR 2014*, pp. 362–366, IEEE, Brussels, doi:10.1109/ICGPR.2014.6970446.
- Di Paolo, F., et al. (2016), Radar signal penetration and horizons detection on Europa through numerical simulations, *IEEE J. Sel. Topics Appl. Earth Observ. Remote Sens.*, 1–12, doi:10.1109/JSTARS.2016.2544103.
- Dombard, A. J., G. W. Patterson, A. P. Lederer, and L. M. Prockter (2013), Flanking fractures and the formation of double ridges on Europa, *Icarus*, 223(1), 74–81, doi:10.1016/j.icarus.2012.11.021.
- Dowdeswell, J. A., and S. Evans (2004), Investigations of the form and flow of ice sheets and glaciers using radio-echo sounding, *Rep. Progr. Phys.*, 67(10), 1821–1861, doi:10.1088/0034-4885/67/10/R03.
- Durham, W. B., L. A. Stern, and S. H. Kirby (2001), Rheology of ice I at low stress and elevated confining pressure, *J. Geophys. Res.*, 106(6), 11031–11042, doi:10.1029/2000JB900446.
- Fujita, S., T. Matsuoka, T. Ishida, K. Matsuoka, and S. Mae (2000), A summary of the complex dielectric permittivity of ice in the megahertz range and its applications for radar sounding of polar ice sheets, in *Physics of Ice Core Records*, edited by T. Hondoh, pp. 185–212, Hokkaido Univ. Press, Sapporo.
- Goldsby, D. L., and D. L. Kohlstedt (2001), Superplastic deformation of ice: Experimental observations, *J. Geophys. Res.*, 106(B6), 11,017–11,030, doi:10.1029/2000JB900336.
- Golombek, M. P., and W. B. Banerdt (1990), Constraints on the subsurface structure of Europa, *Icarus*, 83(2), 441–452, doi:10.1016/0019-1035(90)90078-N.
- Grasset, O., et al. (2013), JUPITER ICY moons Explorer (JUICE): An ESA mission to orbit Ganymede and to characterise the Jupiter system, *Planet. Space Sci.*, 78, 1–21, doi:10.1016/j.pss.2012.12.002.
- Greenberg, R. (1987), Galilean satellites: Evolutionary paths in deep resonance, *Icarus*, 70(2), 334–347, doi:10.1016/0019-1035(87)90139-4.
- Grima, C., D. D. Blankenship, D. A. Young, and D. M. Schroeder (2014), Surface slope control on firm density at Thwaites Glacier, West Antarctica: Results from airborne radar sounding, *Geophys. Res. Lett.*, 41, 6787–6794, doi:10.1002/2014GL061635.
- Grima, C., D. D. Blankenship, and D. M. Schroeder (2015), Radar signal propagation through the ionosphere of Europa, *Planet. Space Sci.*, 117, 421–428, doi:10.1016/j.pss.2015.08.017.
- Gudmandsen, P. (1971), Electromagnetic probing of ice, in *Electromagnetic Probing in Geophysics*, edited by J. R. Wait, pp. 321–348, Golem Press, Boulder, Colo.
- Hand, K. P., C. F. Chyba, J. C. Priscu, R. W. Carlson, and K. H. Nealson (2009), Astrobiology and the potential for life on Europa, in *Europa*, edited by R. T. Pappalardo, W. B. McKinnon, and K. Khurana, pp. 589–629, Univ. of Ariz. Press, Tucson.
- Hansen, C. J., L. Esposito, A. I. F. Stewart, J. Colwell, A. Hendrix, W. Pryor, D. Shemansky, and R. West (2006), Enceladus' water vapor plume, *Science*, 311(5766), 1422–1425, doi:10.1126/science.1121254.
- Hobbs, P. V. (1974), Chapter 5—Thermal properties and Diffusion in Ice.
- Husmann, H., T. Spohn, and K. Wiczekowski (2002), Thermal equilibrium states of Europa's ice shell: Implications for internal ocean thickness and surface heat flow, *Icarus*, 156(1), 143–151, doi:10.1006/icar.2001.6776.
- Kalousová, K., O. Souček, G. Tobie, G. Choblet, and O. Čadež (2014), Ice melting and downward transport of meltwater by two-phase flow in Europa's ice shell, *J. Geophys. Res. Planets*, 119(3), 532–549, doi:10.1002/2013JE004563.

- Kalousová, K., O. Souček, G. Tobie, G. Choblet, and O. Čadež (2016), Water generation and transport below Europa's strike-slip faults, *J. Geophys. Res. Planets*, 121(12), 2444–2462, doi:10.1002/2016JE005188.
- Kargel, J. S., J. Z. Kaye, J. W. Head, G. M. M. III, R. Sassen, J. K. Crowley, O. P. Ballesteros, S. A. Grant, and D. L. Hogenboom (2000), Europa's crust and ocean: Origin, composition, and the prospects for life, *Icarus*, 148(1), 226–265, doi:10.1006/icar.2000.6471.
- Kattenhorn, S. A., and T. Hurford (2009), Tectonics of Europa, in *Europa*, edited by R. T. Pappalardo, W. B. McKinnon, and K. Khurana, pp. 199–236, Univ. of Ariz. Press, Tucson.
- Khurana, K. K., M. G. Kivelson, D. J. Stevenson, G. Schubert, C. T. Russell, R. J. Walker, and C. Polanskey (1998), Induced magnetic fields as evidence for subsurface oceans in Europa and Callisto, *Nature*, 395(6704), 777–780, doi:10.1038/27394.
- Kirk, R. L., and D. J. Stevenson (1987), Thermal evolution of a differentiated Ganymede and implications for surface features (1987), *Icarus*, 69(1), 91–134, doi:10.1016/0019-1035(87)90009-1.
- Kivelson, M. G., K. K. Khurana, C. T. Russell, M. Volwerk, R. J. Walker, and C. Zimmer (2000), Galileo magnetometer measurements: A stronger case for a subsurface ocean at Europa, *Science*, 289(5483), 1340–1343, doi:10.1126/science.289.5483.1340.
- Lide, D. R. (2004), *CRC Handbook of Chemistry and Physics*, 85th ed., CRC Press LLC.
- Logg, A., K. A. Mardal, and G. N. Wells (2012), *Automated Solution of Differential Equations by the Finite Element Method, The FEniCS Book*, Lecture Notes in Computational Science and Engineering, vol. 84, Springer, Berlin.
- MacGregor, J. A., D. P. Winebrenner, H. Conway, K. Matsuoka, P. A. Mayewski, and G. D. Clow (2007), Modeling englacial radar attenuation at Siple Dome, West Antarctica, using ice chemistry and temperature data, *J. Geophys. Res.*, 112, F03008, doi:10.1029/2006JF000717.
- MacGregor, J. A., G. A. Catania, H. Conway, D. M. Schroeder, I. Joughin, D. A. Young, S. D. Kempf, and D. D. Blankenship (2013), Weak bed control of the eastern shear margin of Thwaites Glacier, West Antarctica, *J. Glaciol.*, 59(217), 900–912, doi:10.3189/2013JoG13J050.
- Marion, G. M., and S. A. Grant (1994), FREZCHEM: A chemical-thermodynamic model for aqueous solutions at subzero temperatures, Special Rep. 9418, United States Army, Cold Regions Research and Engineering Laboratory (USACREL), Hanover, N. H.
- Matsuoka, K., J. A. MacGregor, and F. Pattyn (2010), Using englacial radar attenuation to better diagnose the subglacial environment: A review, in *Proceedings of the 13th International Conference on Ground Penetrating Radar (GPR)*, pp. 1–5, IEEE, Lecce, Italy.
- Matsuoka, K., J. A. MacGregor, and F. Pattyn (2012), Predicting radar attenuation within the Antarctic ice sheet, *Earth Planet. Sci. Lett.*, 359, 173–183, doi:10.1016/j.epsl.2012.10.018.
- McCord, T. B., et al. (1998), Salts on Europa's surface detected by Galileo's Near Infrared Mapping Spectrometer, *Science*, 280(5367), 1242–1245, doi:10.1126/science.280.5367.1242.
- McKinnon, W. B. (1999), Convective instability in Europa's floating ice shell, *Geophys. Res. Lett.*, 26(7), 951–954, doi:10.1029/1999GL900125.
- McKinnon, W. B. (2005), Radar sounding of convecting ice shells in the presence of convection: Application to Europa, Ganymede, and Callisto, in *Workshop on Radar Investigations of Planetary and Terrestrial Environments*, vol. 1, 53 pp., Lunar and Planetary Institute, Houston, Tex.
- Mironenko, M. V., S. A. Grant, G. M. Marion, and R. E. Farren (1997), FREZCHEM2: A chemical thermodynamic model for electrolyte solutions at subzero temperatures, CRREL Rep. 97-5, USA Cold Regions Res. and Eng. Lab.
- Mitri, G., and A. P. Showman (2005), Convective-conductive transitions and sensitivity of a convecting ice shell to perturbations in heat flux and tidal-heating rate: Implications for Europa, *Icarus*, 177(2), 447–460, doi:10.1016/j.icarus.2005.03.019.
- Moore, J. C. (2000), Models of radar absorption in European ice, *Icarus*, 147(1), 292–300, doi:10.1006/icar.2000.6425.
- Nimmo, F., B. Giese, and R. T. Pappalardo (2003), Estimates of Europa's ice shell thickness from elastically-supported topography, *Geophys. Res. Lett.*, 30(5), 1233, doi:10.1029/2002GL016660.
- Ojakangas, G. W., and D. J. Stevenson (1989), Thermal state of an ice shell on Europa, *Icarus*, 81(2), 220–241, doi:10.1016/0019-1035(89)90052-3.
- Oswald, G. K. A., and G. D. Q. Robin (1973), Lakes beneath the Antarctic ice sheet, *Nature*, 245, 251–254, doi:10.1038/245251a0.
- Pappalardo, R. T., et al. (1999), Does Europa have a subsurface ocean? Evaluation of the geological evidence, *J. Geophys. Res.*, 104(E10), 24,015–24,055, doi:10.1029/1998JE000628.
- Pappalardo, R. T., and A. C. Barr (2004), The origin of domes on Europa: The role of thermally induced compositional diapirism, *Geophys. Res. Lett.*, 31, L01701, doi:10.1029/2003GL019202.
- Pappalardo, R., D. Senske, L. Prockter, B. Paczkowski, S. Vance, A. Rhoden, B. Goldstein, T. Wagner, and B. Cooke (2015), *Science Objectives for the Europa Clipper Mission Concept: Investigating the Potential Habitability of Europa*, European Planetary Science Congress, vol. 10, EPSC Abstracts, EPSC2015-156, Nantes, France.
- Peters, M. E., D. D. Blankenship, S. P. Carter, S. D. Kempf, D. A. Young, and J. W. Holt (2007), Along-track focusing of airborne radar sounding data from West Antarctica for improving basal reflection analysis and layer detection, *IEEE Trans. Geosci. Remote Sens.*, 45(9), 2725–2736, doi:10.1109/TGRS.2007.897416.
- Pettinelli, E., B. Cosciotti, F. Di Paolo, S. E. Lauro, E. Mattei, R. Orosei, and G. Vannaroni (2015), Dielectric properties of Jovian satellite ice analogs for subsurface radar exploration: A review, *Rev. Geophys.*, 53(3), 593–641, doi:10.1002/2014RG000463.
- Phillips, R. J., et al. (2008), Mars north polar deposits: Stratigraphy, age, and geodynamical response, *Science*, 320(5880), 1182–1185, doi:10.1126/science.1157546.
- Picardi, G., et al. (2005), Radar soundings of the subsurface of Mars, *Science*, 310(5756), 1925–1928, doi:10.1126/science.1122165.
- Plaut, J. J., et al. (2007), Subsurface radar sounding of the south polar layered deposits of Mars, *Science*, 316(5821), 92–95, doi:10.1126/science.1139672.
- Richardson, C. (1976), Phase relationships in sea ice as a function of temperature, *J. Glaciol.*, 17(77), 507–519, doi:10.3198/1976JoG17-77-507-519.
- Roth, L., J. Saur, K. D. Retherford, D. F. Strobel, P. D. Feldman, M. A. McGrath, and F. Nimmo (2014), Transient water vapor at Europa's south pole, *Science*, 343(171), doi:10.1126/science.1247051.
- Schmidt, B. E., D. D. Blankenship, G. W. Patterson, and P. M. Schenk (2011), Active formation of chaos terrain over shallow subsurface water on Europa, *Nature*, 479(7374), 502–505, doi:10.1038/nature10608.
- Schroeder, D. M., D. D. Blankenship, D. A. Young, A. E. Witus, and J. B. Anderson (2014), Airborne radar sounding evidence for deformable sediments and outcropping bedrock beneath Thwaites Glacier, West Antarctica, *Geophys. Res. Lett.*, 41, 7200–7208, doi:10.1002/2014GL061645.
- Schroeder, D. M., C. Grima, and D. D. Blankenship (2016), Evidence for variable grounding-zone and shear-margin basal conditions across Thwaites Glacier, West Antarctica, *Geophysics*, 81(1), WA35–WA43, doi:10.1190/geo2015-0122.1.
- Seu, R., et al. (2007), SHARAD sounding radar on the Mars Reconnaissance Orbiter, *J. Geophys. Res.*, 112, E05505, doi:10.1029/2006JE002745.
- Showman, A. P., and L. Han (2004), Numerical simulations of convection in Europa's ice shell: Implications for surface features, *J. Geophys. Res.*, 109, E01010, doi:10.1029/2003JE002103.

- Showman, A. P., and L. J. Han (2005), Effects of plasticity on convection in an ice shell: Implications for Europa, *Icarus*, 177(2), 425–437, doi:10.1016/j.icarus.2005.02.020.
- Sotin, C., G. Tobie, J. Wahr, and W. B. McKinnon (2009), Tides and tidal heating on Europa, in *Europa*, edited by R. T. Pappalardo, W. B. McKinnon, and K. Khurana, pp. 85–117, Univ. of Ariz. Press, Tucson.
- Sparks, W. B., K. P. Hand, M. A. McGrath, E. Bergeron, M. Cracraft, and S. E. Deustua (2016), Probing for evidence of plumes on Europa with HST/STIS, *Astrophys. J.*, 829(2), 121, doi:10.3847/0004-637X/829/2/121.
- Taylor, C., and P. Hood (1973), A numerical solution of the Navier-Stokes equations using the finite element technique, *Comput. Fluids*, 1(1), 73–100, doi:10.1016/0045-7930(73)90027-3.
- Tobie, G., G. Choblet, and C. Sotin (2003), Tidally heated convection: Constraints on Europa's ice shell thickness, *J. Geophys. Res.*, 108(E11), 5124, doi:10.1029/2003JE002099.
- Tobie, G., O. Grasset, J. I. Lunine, A. Mocquet, and C. Sotin (2005), Titan's internal structure inferred from a coupled thermal-orbital model, *Icarus*, 175(2), 496–502, doi:10.1016/j.icarus.2004.12.007.
- Williams, K. K., and R. Greeley (1998), Estimates of ice thickness in the Conamara Chaos region of Europa, *Geophys. Res. Lett.*, 25(23), 4273–4276, doi:10.1029/1998GL900144.
- Zolotov, M. Y., and E. L. Shock (2001), Composition and stability of salts on the surface of Europa and their oceanic origin, *J. Geophys. Res.*, 106(E12), 32815–32827, doi:10.1029/2000JE001413.
- Zolotov, M. Y., and J. S. Kargel (2009), On the composition of Europa's icy shell, ocean and underlying rocks, in *Europa*, edited by R. T. Pappalardo, W. B. McKinnon, and K. Khurana, pp. 431–457, Univ. of Ariz. Press, Tucson.